Gigayear stability of cratonic edges controls global distribution of sediment-hosted metals

Karol Czarnota*[,1,2], Mark J. Hoggard*[,3,4], Fred D. Richards[3], David L. Huston[1] & A. Lynton Jaques[2]

1. Geoscience Australia, GPO Box 378, Canberra ACT 2601, Australia.
2. Research School of Earth Sciences, Australian National University, Canberra, ACT 0200, Australia
3. Department of Earth and Planetary Sciences, Harvard University, 20 Oxford Street, Cambridge, MA 02138, USA.
4. Lamont-Doherty Earth Observatory, Columbia University, 61 Rte 9W, Palisades, NY 10964, USA.

*karol.czarnota@ga.gov.au; mark_hoggard@fas.harvard.edu

Add proper acknowledgment of ACS and define tau prime eta and tau s in the anelasticity section.

Sustainable development and transition to a clean-energy economy is placing ever-increasing demand on global supplies of base metals (copper, lead, zinc and nickel). Alarmingly, this demand is outstripping the present rate of discovery of new deposits, with significant shortfalls forecast in the coming decades. Thus, to maintain growth in global living standards, dramatic improvements in exploration success rate are an essential goal of the geoscience community. Significant quantities of base metals have been deposited by low-temperature hydrothermal circulation within sedimentary basins over the last 2 billion years. Despite over a century of research, relationships between these deposits and geological structures remain enigmatic. Here, for the first time, we show that 85% of sediment-hosted base metals, including all giant deposits (>10 megatonnes of metal), occur within 200 km of the edges of thick lithosphere, mapped using surface wave tomography and a parameterisation for anelasticity at seismic frequencies. This remarkable observation implies long-term lithospheric edge stability and a genetic link between deep Earth processes and near-surface hydrothermal mineral systems. This result provides an unprecedented global framework for identifying fertile regions for targeted mineral exploration, reducing the search-space for new deposits by two-thirds on this lithospheric thickness criterion alone.

Consumption of base metals over the next ∼25 years is set to exceed the total produced in human history to date.[1,2] Moreover, trace metals (e.g. cobalt, indium and germanium) are often produced as by-products of base metal mining and are essential in many high-tech applications.[3] A growing concern is that the rate of exploitation of existing reserves is outstripping discovery of new deposits, despite exploration expenditure tripling during the 2005–2012 minerals boom.[1,2] To reverse this worrying trend, improved techniques for locating new deposits are required, particularly those buried under shallow sedimentary cover or ice. Initial area selection at continental scales is arguably the most important stage of mineral exploration, as successful identification of fertile regions can compensate for many subsequent exploration errors.[4]

Global Deposit Classification

Over the last two decades, ore deposit research has progressed from documentation and classification towards a more holistic understanding of factors controlling generation and preservation of mineral deposits.[5,6] Classification schemes have identified six major base metal deposit types, based on variations in mineral assemblages, host lithology, structural architecture and geological setting. Three of these are associated with magmatic processes: porphyry copper (contains ∼65% of all known copper); magmatic nickel-copper-platinum group elements (∼45% nickel, ∼3% copper); and volcanic-hosted massive sulphide copper-lead-zinc (∼6% copper, ∼23% lead, ∼39% zinc). Mineral systems analysis has resulted in a growing acceptance that the spatial distribution of such deposits associated with magmatic processes is controlled by lithospheric-scale structure.[4,7,8]

The other three deposit types are associated with low-temperature hydrothermal circulation in sedimentary basins: sedimentary copper (Cu-sed; contains ∼20% of all known copper); clastic-dominated lead-zinc (PbZn-CD), commonly also referred to as sedimentary exhalative (∼43% of all lead and ∼33% of zinc); and Mississippi Valley-type lead-zinc (PbZn-MVT; ∼25% lead, ∼22% zinc). Most assessments to date have focused on the genesis of these sediment-hosted deposits within the context of Earth's secular evolution as well as past tectonic and geographic settings.[9,10,11,12] However, the first-order geological control on their spatial distribution throughout the continents is unknown, severely limiting predictive power for identifying new targets. A classic example comes from the Carpentaria Zinc Belt in northern Australia, which contains several world class PbZn-CD deposits formed between 1.8–1.4 Ga (Figure 1a). These deposits lie along an arcuate trend that runs oblique to mapped geology and crustal geological boundaries, as demonstrated by gravity and magnetic datasets.[13] This linear distribution hints at an underlying regional-scale control. Given the absence of a clear crustal relationship, we therefore investigate both regional and global-scale links between base-metal deposits and the most fundamental shallow mantle structure – the lithosphere-asthenosphere boundary (LAB).

Relationship with Lithospheric Structure

We begin by collating global inventories of the six aforementioned major base-metal systems from published sources (Supplementary Information). We next refine a method[14] for mapping the thermal LAB from seismic tomography, taking into consideration recent laboratory experiments[15] concerning the effect of anelasticity on shear-wave velocities (Methods). This benchmarking procedure is necessary due to substantial variability in the results of different tomography models. A high resolution regional map over Australia is obtained from the `FR12` model[16] and is calibrated using nine local paleogeotherms derived from thermobarometry of mantle peridotite xenoliths and xenocrysts. To expand our analysis to other continents, a global LAB is also produced using `SL2013sv` tomography[17] and calibrated using multiple constraints, including the latest thermal structure of cooling oceanic lithosphere.[18] This global LAB exhibits a bi-modal thickness distribution, with peaks at 80 km and 180 km, separated by a minimum at 150 km (Supplementary Information).

Inspection of the Australian model reveals a striking correlation between major sediment-hosted mineral deposits and the edge of thick lithosphere, defined here by the 170 km thickness contour (Figure 1b). Major PbZn-CD and sedimentary copper deposits in the Carpentaria Zinc Belt overlie this contour, which runs obliquely to geological boundaries, such that intersections between these two features consistently coincide with deposit locations. This behaviour is particularly useful for highlighting new prospective regions for exploration. Other observables that correlate with this lithospheric thickness change include variations in lead isotopes from Proterozoic galena and pyrite minerals,[19] a topographic ridge and the western extent of Cretaceous marine sediments (Figure 1a). These latter two associations demonstrate the post-Proterozoic stability of this edge and its influence on local geology and topography. There is also a strong relationship with iron-oxide-copper-gold deposits, including the Olympic Dam mine in south Australia (84 Mt of copper, largest known uranium resource). However, lack of consensus over global classification schemes means that we have limited analysis of this deposit type to Australia.

Extension to a global analysis confirms the strength of this relationship (Figure 2). There is a remarkable link between the 170 km lithospheric thickness contour and location of large deposits that holds regardless of deposit age, which spans at least the last 2 billion years. Surprisingly, given results of previous studies,[8] deposits associated with magmatic systems generally do not follow this simple pattern (Supplementary Information).

To quantify these visual relationships, the shortest distance is calculated between each deposit and the 170 km LAB thickness contour and results are plotted in a cumulative distribution function (CDF). Weighting deposits by the mass of contained metal and substituting the Australian LAB from the global model with our regionally enhanced version substantially improves the correlation for PbZn-CD (Figure 3a). Globally, we observe that $\sim 90\%$ of sedimentary copper, $\sim 90\%$ of clastic-dominated lead-zinc and $\sim 70\%$ of Mississippi Valley-type lead-zinc resources are located within 200 km of the 170 km LAB thickness contour (Figure 3b). This region corresponds to only $\sim 36\%$ of continental surface area. Given that this swath width is similar to the ~ 280 km node spacing in SL2013sv, tighter constraints are only possible with higher resolution tomography models. The significance of this result is examined using the *two-sample Kolmogorov-Smirnov test*[20] which estimates that the probability of these sediment-hosted deposits representing random continental locations is less than 1 in 10^{12} (Methods).

Despite this general association, there are some notable exceptions. Minor PbZn-CD outliers occur in Europe, the Caribbean, Indonesia and east China. Anomalous PbZn-MVT deposits are found in Ireland, east China and along the Tethys subduction zone across Europe, whilst minor sedimentary copper deposits occur in southwestern North America and southern South America. Not all outliers were necessarily anomalies at the time of ore formation. The majority now occur in accretionary terranes, whereby plate tectonic processes may have rifted segments off thick lithosphere and transported them into subduction zone settings. Other areas, such as east China, are known to have undergone lithospheric thinning some time after deposit formation, based on thermobarometric constraints.[21]

Regardless of age, sediment-hosted base-metal deposits predominantly cluster on the edges of present-day thick lithosphere. Therefore, many of these lithospheric steps appear to be remarkably robust on billion-year timescales, despite the assembly and disaggregation of several supercontinents, impacts of large igneous provinces and the erosional effect of edge-driven convection. Deposits in northwestern North America span ages $\sim$ 1.5–0.5 Ga, pointing to the stability and importance of this boundary in localising multiple deformation and ore-forming processes.

Mineral System Implications

The majority of sediment-hosted base metal deposits are found in failed rift and passive margin settings.[9,10] Our results indicate that the edges of thick lithosphere place first-order controls on the genesis of these extensional basins and their associated mineral systems (Figure 4). It is generally agreed that basin-scale hydrothermal circulation is required to scavenge sufficient metals to form giant deposits.[22] Metals are mobilised and transported by oxidised brines with moderate temperatures (80–250°C) and moderate-to-high salinity (10–30 wt.% NaCl), limiting their maximum age to the Great Oxidation Event at 2.4 Ga.[9,10] These fluids are sourced from evaporites at low latitudes and remain buffered as they pass through voluminous oxidised terrestrial sediments, allowing them to scavenge lead from arkosic sandstones and felsic volcanics, as well as copper and zinc from mafic rocks.[9,10] The latter are more prevalent in distal parts of the basin where extension and decompression melting rates are greatest. Transport along faults focuses these fluids into oxidation-reduction interfaces, such as distal-facies black shales, where metals precipitate.[11] The optimal juxtaposition of these elements for efficient mineralisation is fundamentally controlled by the lithospheric thickness change imparted by rifting. This transition marks the confluence between oxidising terrestrial environments on thick lithosphere and reducing marine settings above thinner lithosphere. The adjacent cratons provide a bountiful source of oxidised sediments and extensive low-elevation platforms that enhance evaporite formation. Proximal land masses also promote restricted marine settings that are favourable for euxinic water conditions and deposition of reducing shales high in organic carbon. Metal precipitation at these sites is ineffective when fluid temperatures exceed $\sim$ 250°C.[11] Reduced geothermal gradients associated with thicker lithosphere extend the depth range for sourcing brines cooler than this threshold, thereby maximising the depth extent of the metal scavenging window.

From a geodynamical perspective, these lithospheric edges represent rheological contrasts that focus strain and localise repeated cycles of extensional deformation and basin contraction, thereby controlling both the spatial distribution of required lithologies and the focusing of mineralising fluids.[23,24] Intercalation of necessary proximal and distal facies components is further modulated by transient vertical motions, generally thought to be associated with edge driven convection across lithospheric steps.[25] Finally, a setting on the edge of thick lithosphere enhances the preservation potential of deposits through subsequent orogenic events and supercontinent cycles. For example, the 1.7 Ga Broken Hill deposit in Australia (world's largest lead deposit) has been metamorphosed to amphibolite–granulite facies, yet survives on the edge of the Curnamona part of the South Australian Craton.

In contrast to sediment-hosted base-metals, magmatic deposits do not show such a strong association with the edge of thick lithosphere (Supplementary Material). Porphyry copper deposits are predominantly Cenozoic in age and generally on thin lithosphere ($\leq$100 km). Their formation in subduction zone settings at shallow crustal depths leads to poor preservation potential within the geological record, making this association unsurprising. Volcanogenic massive sulphides have a relatively continuous, though pulsed, age distribution from 3.5 Ga to present.

Their generation is thought to require moderate-degree partial melting of hydrated mantle in back-arc settings.[26] We observe that they spatially occur randomly on thick and thin lithosphere, but exhibit systematic temporal ordering, with the oldest positioned over thick lithosphere rimmed by progressively younger deposits, consistent with growth of cratons by accretion. Finally, magmatic nickel deposits are mostly Archean and Proterozoic in age and commonly occur on thick lithosphere ($\geq$150 km). Unlike other base metal deposits, their distribution is associated with edges of even thicker lithosphere ($\sim$ 200 km), broadly consistent with previous studies showing major lithospheric structural controls on deposit locations.[7] Their generation requires large fraction partial melting of peridotite, indicative of high mantle temperatures (more prevalent in a early, hotter Earth) and decompression melting at shallow depths.[27] Therefore, their present distribution suggests lithospheric thickness must have locally increased since formation, simultaneously enhancing preservation potential.

In summary, this work illustrates a new and remarkably clear link between giant sediment-hosted base metal mineral systems and the edges of thick lithosphere. Approximately 55% of the world's lead, 45% of its zinc and 20% of known copper is found within $\sim$200 km of this edge. We have demonstrated the value of regional seismic arrays to better resolve this edge and enhance the mineral exploration efforts required to sustain ongoing global development. Significantly, deposit ages indicate that, following rifting, edges of thick-lithosphere are generally stable over billion-year timescales. The far-reaching geodynamic and societal implications of our observations highlight the urgent need for further research. To improve resolution of mapped lithospheric structure, higher fidelity seismic imaging must be coupled with enhanced mantle xenolith coverage and tighter constraints on seismic anelasticity from mineral physics experiments. More generally, these maps need to be integrated with models of basin dynamics, surface processes and reactive transport modelling, and bench-marked against additional geological information, such as sedimentary facies variations, tectonic structures and alteration zones. These multiple research strands will yield fundamental new insights into sediment-hosted mineral systems and lead to substantial improvements in exploration success rates.

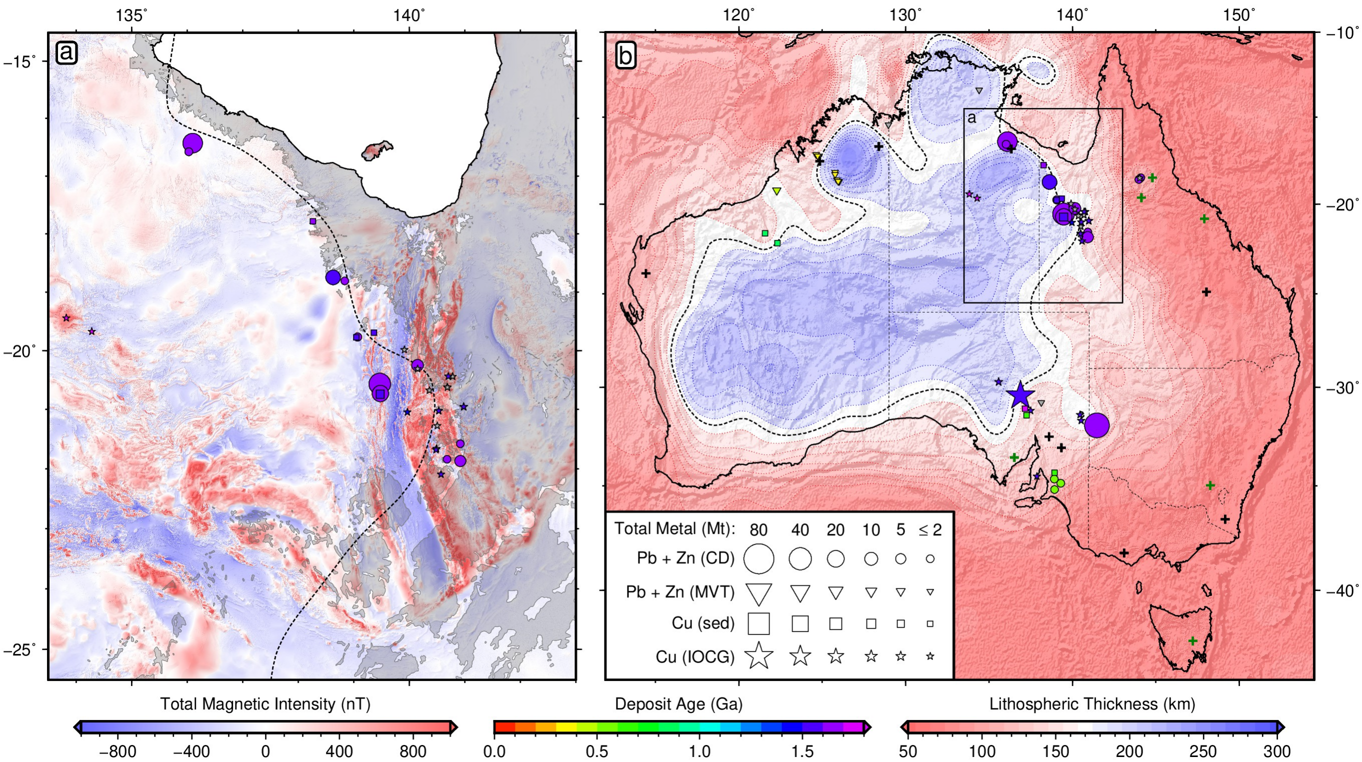

Figure 1: **Distribution of sediment-hosted and iron-oxide-copper-gold base metal deposits as a function of lithospheric thickness in Australia.** (a) Carpentaria Zinc Belt; red/blue = variably reduced to pole aeromagnetic intensity data [13]; grey polygons = generalised outcrop of Cretaceous marine sediments in Eromanga and Karumba Basins [28]; black dashed contour = 170 km LAB thickness; symbols = deposit locations; area proportional to estimate of total contained mass of metal (Mt = megatonnes); unknown deposit size given 2 Mt symbol; colour = ore body formation age (billion years); unknown age plotted in grey; circles = clastic-dominated lead-zinc (PbZn-CD); triangles = Mississippi Valley type lead-zinc (PbZn-MVT); squares = sedimentary copper (Cu-sed); stars = iron-oxide-copper-gold (IOCG). (b) LAB mapped by converting FR12 tomography [16] to temperature using an anelasticity parameterisation [15] calibrated on local paleogeotherms (Supplementary Material) and illuminated by free-air gravity anomalies [13]; black/green crosses = geotherms used as constraints/tests in anelasticity calibration; box = location of panel (a).

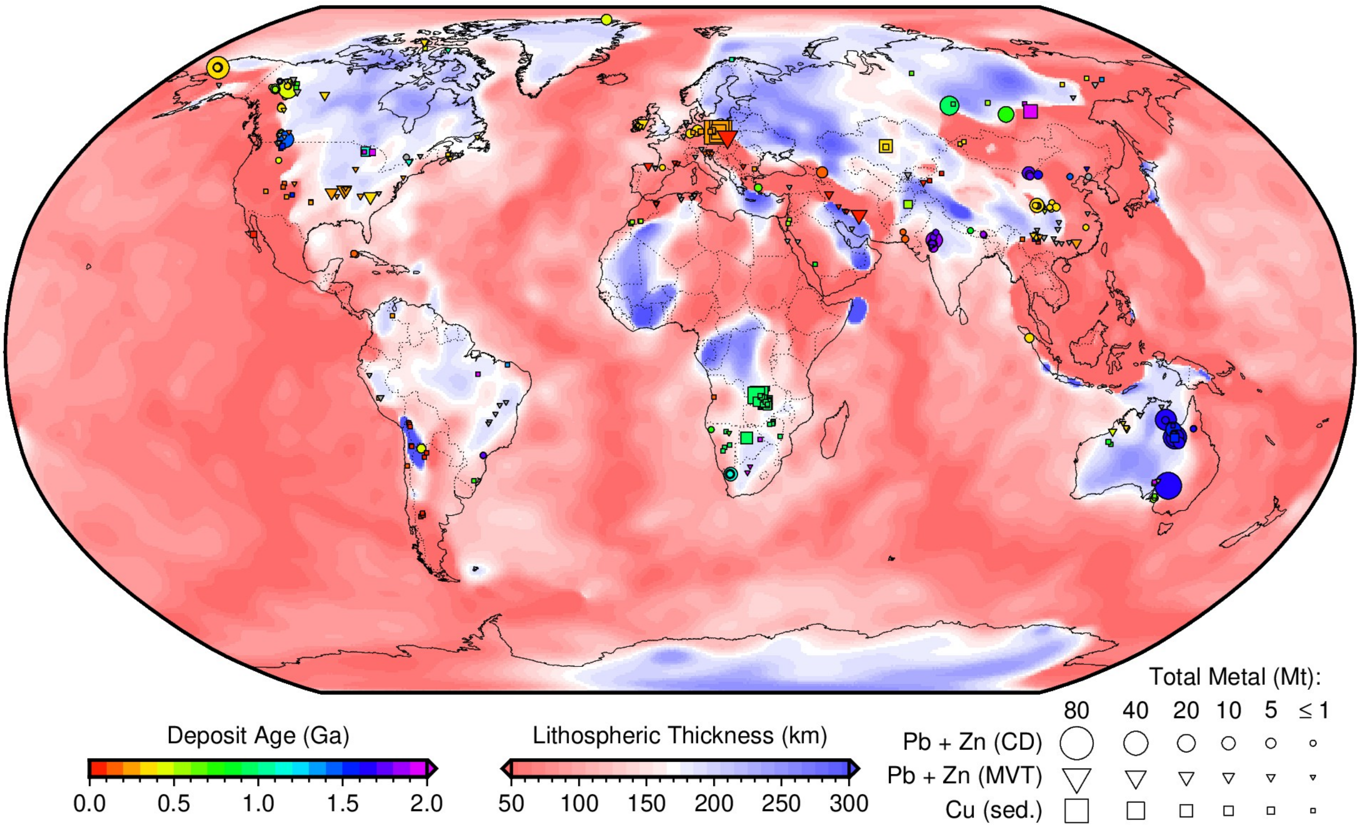

Figure 2: **Global distribution of sediment-hosted base metal deposits as a function of lithospheric thickness.** LAB derived from SL2013sv tomography model[17] using a calibrated anelasticity parameterisation[15] (Methods). Symbols = deposit locations; area proportional to estimate of total contained mass of metal (Mt = megatonnes); unknown deposit size given 1 Mt symbol; colour = ore body formation age (billion years); unknown age plotted in grey; circles = clastic-dominated lead-zinc (PbZn-CD); triangles = Mississippi Valley type lead-zinc (PbZn-MVT); squares = sedimentary copper (Cu-sed).

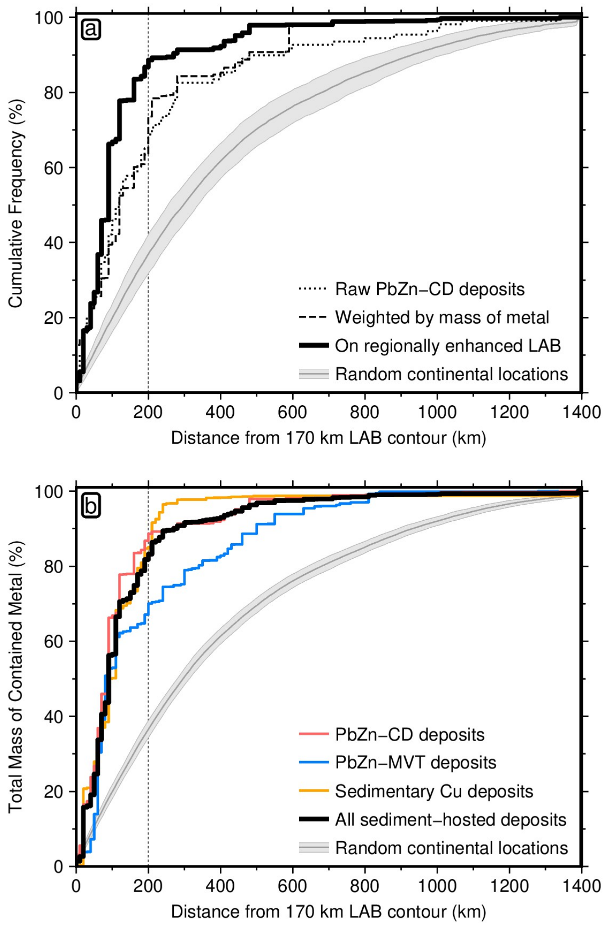

Figure 3: **Cumulative distribution functions for global sediment-hosted base metals.** (a) Different approaches for counting 109 clastic-dominated lead-zinc deposits (PbZn-CD). Dotted line = simple count of number of deposits with increasing distance from the 170 km contour in global LAB map (Figure 2); dashed line = weighting by contained mass of lead and zinc; solid black line = mass-weighted deposits where the Australian LAB has been replaced with the regionally enhanced map (Figure 1b); grey line/bounds = mean and standard deviation of 100 sets of equivalent number of randomly drawn continental locations, with respect to regionally enhanced LAB. (b) Weighted, regionally enhanced CDFs for 109 PbZn-CD, 147 Mississippi Valley-type (PbZn-MVT), 139 sedimentary copper (Cu-sed) and combination of all three. Grey band as before for combined database.

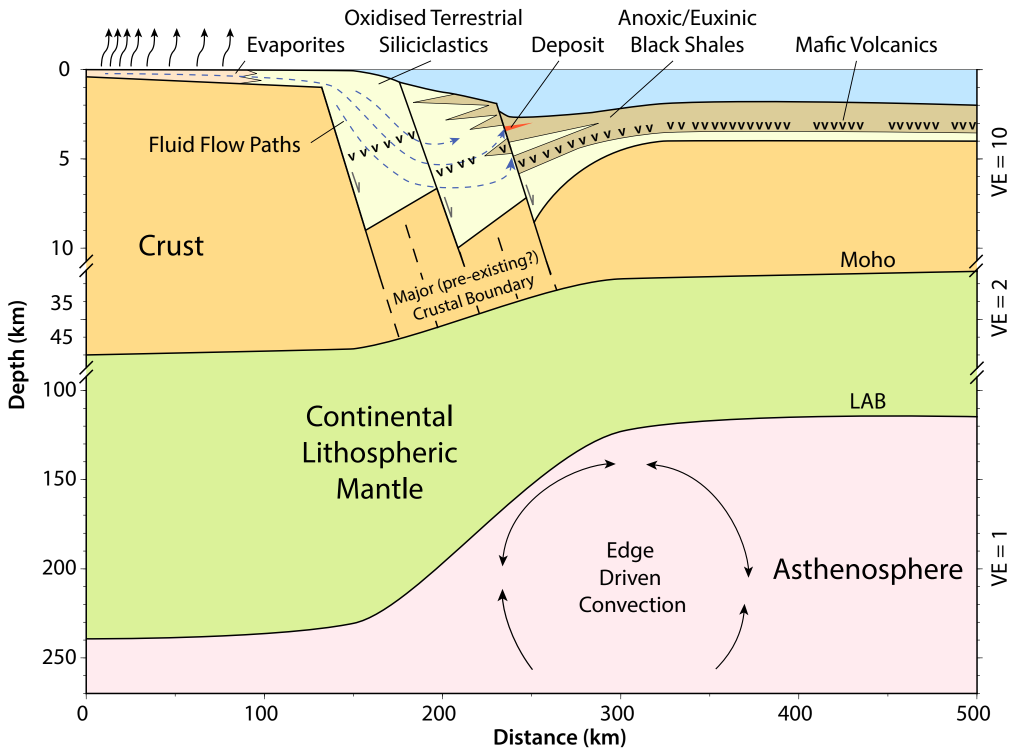

Figure 4: **Schematic illustration of sediment-hosted base metal deposit genesis in extensional settings.** Influence of lithospheric edge on mineral system components during rifting. Basinal brines sourced from evaporites scavenge metals from oxidised terrestrial sediments and volcanics (v) on route to metal deposition sites in black shales.[22] Notice variable vertical exaggeration (VE) and prominence of the lithosphere-asthenosphere boundary edge illustrated at 1:1 scale. Schematic based on architectural constraints from the Australian Carpenteria Zinc Belt and Polish Fore-Sudetic Block.

Methods

Deposit compilation. Our global inventory of 2141 major base metal deposits are categorised into six classes. Three are sediment hosted: sedimentary copper (Cu-sed); clastic-dominated lead-zinc (PbZn-CD); and Mississippi Valley-type lead-zinc (PbZn-MVT). The other three are associated with magmatic systems: copper porphyry (Cu-por); magmatic nickel-copper-platinum group elements (Ni-Cu-PGE); and volcanogenic massive sulfides (VMS). For each deposit, we include the type (based on established classification schemes), location, age (direct measurement or inferred based on geological relationships) and total resource size by combining historical production with estimated resources. Our Cu-sed deposit dataset follows the classification scheme and compilation of Hitzman et al. (2005), cross-checked against Cox et al. (2007).[29,30]. Where these two compilations disagree on deposit size, the larger value has been used. Our PbZn-CD and PbZn-MVT deposit compilations extensively revise and build on the work of Taylor et al. (2009).[31] References for each deposit type were manually checked and additional references have been included. We exploit the compilation of Sillitoe (2010) for Cu-por deposits.[32] Our magmatic Ni-Cu-PGE compilation follows Hoatson et al. (2006), with deposit location populated from disparate sources.[33] Our catalogue of VMS deposits is an extensive revision of the compilation by Franklin et al. (2005).[34] Australian information for all the above deposit types, with the addition of 25 iron-oxide-copper-gold deposits, was updated using the authors' own knowledge, building on the Geoscience Australia OZMin database.[35] We have endeavoured to assemble the most complete deposit dataset possible by revising and extending pre-existing compilations (Supplementary Information). Importantly, patchy or absent reporting of mineral deposit information from some countries inevitably means our global database is incomplete, but we do not believe that this will impact the veracity of our main conclusions.

Choice of seismic tomography model. Our LAB maps are based on the most recent, high-resolution shear wave tomography models. For the global map, we use SL2013sv[17] which is an upper mantle-only model built from a combination of body and surface waves, including fundamental and higher modes. Periods considered are 11–450 s, $\sim 750,000$ seismograms are included, and misfits are calculated between synthetics and the full waveform up to the 9^{th} overtone. Crucially, simultaneous inversion for the crustal model results in minimal smearing of slow crustal velocities down into the upper mantle, thereby allowing us to use more depth slices in our V_S to temperature calibration. Checkerboard resolution tests indicate that features ~ 600 km in diameter at lithospheric depths are generally well resolved. Finer features should be resolvable in regions with dense ray path coverage, such as North America, Europe and southeast Asia. The SL2013sv model contains only 6 seismometers in Australia, so has limited resolution within this continent. Therefore, we also investigate the FR12 regional seismic tomography model[16] to generate a high resolution map for the Australian continent. FR12 is a radially isotropic V_S model derived from Rayleigh wave travel times.[36] Periods considered are 50–120 s and the fundamental and first four higher modes have been used where possible, leading to good sensitivity down to ~ 250 km depths. It contains a greater number of source–receiver paths ($> 13,000$) compared to other Australian models. However, it uses an *a priori* crustal model that remains fixed throughout the inversion, resulting in noticeable smearing of crustal velocities into the upper mantle. Checkerboard tests indicate that features ~ 300 km in diameter at lithospheric depths are well resolved.

Parameterising shear-wave anelasticity. For converting shear-wave velocities (V_S) to temperature, we adopt the parameterisation of Yamauchi & Takei (2016)[15], which includes effects of anelasticity in pre-melt conditions (temperatures above $\sim 90\%$ of melting temperature). V_S is defined as

$$V_S = \frac{1}{\sqrt{\rho J_1}} \left(\frac{1 + \sqrt{1 + (J_2/J_1)^2}}{2} \right)^{-\frac{1}{2}} \simeq \frac{1}{\sqrt{\rho J_1}} \tag{1}$$

where ρ is the density and J_1 and J_2 represent real and imaginary components of the complex compliance, J^*, which is a quantity describing the sinusoidal strain resulting from the application of a unit sinusoidal stress. J_1 represents the strain amplitude in phase with the driving stress, whilst the J_2 component is $\frac{\pi}{2}$ out of phase, resulting in dissipation. These terms are expressed as

$$J_1(\tau_S') = J_U \left[1 + \frac{A_B [\tau_S']^{\alpha_B}}{\alpha_B} + \frac{\sqrt{2\pi}}{2} A_P \; \sigma_P \left\{ 1 - \mathrm{erf}\left(\frac{\ln[\tau_P'/\tau_S']}{\sqrt{2}\sigma_P} \right) \right\} \right] \tag{2}$$

$$J_2(\tau_S') = J_U \frac{\pi}{2} \left[A_B [\tau_S']^{\alpha_B} + A_P \; \exp\left(-\frac{\ln^2[\tau_P'/\tau_S']}{2\sigma_P^2} \right) \right] + J_U \tau_S' \tag{3}$$

where $A_B = 0.664$ and $\alpha_B = 0.38$ represent the amplitude and slope of background stress relaxation and J_U is the unrelaxed compliance. Parameters A_P and σ_P represent the amplitude and width of a high frequency relaxation peak superimposed on this background trend such that

$$A_P(T') = \begin{cases} 0.01 & \text{for } T' < 0.91 \\ 0.01 + 0.4(T' - 0.91) & \text{for } 0.91 \leq T' < 0.96 \\ 0.03 & \text{for } 0.96 \leq T' < 1 \\ 0.03 + \beta(\phi_m) & \text{for } T' \geq 1 \end{cases} \tag{4}$$

and

$$\sigma_P(T') = \begin{cases} 4 & \text{for } T' < 0.92 \\ 4 + 37.5(T' - 0.92) & \text{for } 0.92 \leq T' < 1 \\ 7 & \text{for } T' \geq 1 \end{cases} \tag{5}$$

where T' is homologous temperature ($\frac{T}{T_s}$) with T the temperature and T_s the solidus temperature, both in Kelvin. ϕ_m is the melt fraction and $\beta(\phi_m)$ describes the direct poroelastic effect of melt (assumed to be negligible under upper mantle conditions). For this case, J_U is the inverse of the unrelaxed shear modulus, $\mu_U(P,T)$, such that

$$J_U(P,T)^{-1} = \mu_U(P,T) = \mu_U^0 + \frac{\partial \mu_U}{\partial T}(T - T_0) + \frac{\partial \mu_U}{\partial P}(P - P_0) \tag{6}$$

where μ_U^0 is the unrelaxed shear modulus at surface pressure-temperature conditions, the differential terms are assumed to be constant and the pressure, P, in GPa is linearly related to the depth, z, in km by $\frac{z}{30}$. The normalised shear wave period, τ_S', in Equations (2) and (3) is equal to $\frac{\tau_S}{2\pi\tau_M}$, where τ_S is the shear wave period and $\tau_M = \frac{\eta}{\mu_U}$ is the normalised Maxwell relaxation timescale. τ'_P represents the normalised shear-wave period associated with the centre of the high frequency relaxation peak, assumed to be 6×10^{-5}. The shear viscosity, η, is

$$\eta = \eta_r \left(\frac{d}{d_r}\right)^m \exp\left[\frac{E_a}{R}\left(\frac{1}{T} - \frac{1}{T_r}\right)\right] \exp\left[\frac{V_a}{R}\left(\frac{P}{T} - \frac{P_r}{T_r}\right)\right] A_\eta \tag{7}$$

where d is the grain size, m the grain size exponent (assumed to be 3), R the gas constant, E_a the activation energy and V_a the activation volume. Subscripts $[X]_r$ refer to reference values, assumed to be $d_r = d = 1$ mm, $P_r = 1.5$ GPa and $T_r = 1200$°C for the upper mantle. A_η represents the extra reduction of viscosity due to an increase in E_a near the solidus, expressed as

$$A_\eta(T') = \begin{cases} 1 & \text{for } T' < T'_\eta \\ \exp\left[-\frac{(T'-T'_\eta)}{(T'-T'T'_\eta)}\ln(\gamma)\right] & \text{for } T'_\eta \leq T' < 1 \\ \gamma^{-1}\exp(\lambda\phi) & \text{for } T' \geq 1 \end{cases} \tag{8}$$

where T'_η is the homologous temperature above which activation energy becomes $E_a + \Delta E_a$ and $\gamma = 5$ is the factor of additional reduction. $\lambda\phi$ describes the direct effect of melt on viscosity, assumed to be negligible here. The solidus temperature, T_s, is fixed to a value of 1326°C at 50 km equivalent to a dry peridotite solidus[37] and linearly increases below this depth according to

$$T_s(z) = 1599 + \frac{\partial T_s}{\partial z}(z - 50 \text{ km}) \tag{9}$$

where $\frac{\partial T_s}{\partial z}$ is the solidus gradient. We use a temperature-dependent, compressible density, $\rho(P, T)$, following the approach of Grose & Afonso (2013).[38] First, we define a linear temperature-dependence on thermal expansivity, $\alpha(T)$, such that

$$\alpha(T) = \alpha_0 + \alpha_1 T \tag{10}$$

where $\alpha_0 = 2.832 \times 10^{-5}$ °C^{-1} and $\alpha_1 = 0.758 \times 10^{-8}$ °C^{-2} are constants calibrated from mineral physics experiments. To include pressure-dependence, the isothermal volume change, $(V_0/V)_T$ is calculated at each pressure using a Brent minimisation algorithm and the third-order Birch-Murnaghan equation of state

$$P = \frac{3}{2}K_0\left[\left(\frac{V_0}{V}\right)_T^{\frac{7}{3}} - \left(\frac{V_0}{V}\right)_T^{\frac{5}{3}}\right]\left\{1 + \frac{3}{4}(K'_T - 4)\left[\left(\frac{V_0}{V}\right)_T^{\frac{2}{3}} - 1\right]\right\} \tag{11}$$

where $K_0 = 130$ GPa is the bulk modulus at zero pressure and $K'_T = 4.8$ is the pressure-derivative of the isothermal bulk modulus. The associated isothermal density change with pressure, $\rho(P)$, is given by

$$\rho(P) = \rho_0 \left(\frac{V_0}{V}\right)_T \tag{12}$$

where $\rho_0 = 3.33$ Mg m^{-3} is the density of mantle at surface pressure and temperature. The effect of pressure on thermal expansivity is included according to

$$\frac{\alpha(P,T)}{\alpha(T)} = \left(\frac{V_0}{V}\right)_T \exp\left\{(\delta_T + 1)\left[\left(\frac{V_0}{V}\right)_T^{-1} - 1\right]\right\} \tag{13}$$

where $\delta_T = 6$ is the Anderson-Grüneisen parameter. Thus, the final density, $\rho(P,T)$, can be calculated using

$$\rho(P,T) = \rho_0 \left(\frac{V_0}{V}\right)_T \left\{1 - \left[\frac{\alpha(P,T)}{\alpha(T)}\right]\left[\alpha_0(T - T_0) + \frac{\alpha_1}{2}(T^2 - T_0^2)\right]\right\} \tag{14}$$

where $T_0 = 273$ K is temperature at the surface. In a similar manner to Equation (1), the shear-wave attenuation, Q_S^{-1}, can be defined as

$$Q_S^{-1} = \frac{J_2}{J_1}\left(\frac{1 + \sqrt{1 + (J_2/J_1)^2}}{2}\right)^{-1} \simeq \frac{J_2}{J_1} \tag{15}$$

Xenolith and xenocryst thermobarometry. Temperature estimates across a range of depths are required to generate a series of V_S-T-P tie points in order to calibrate the regional seismic tomography models. We therefore assemble a suite of fifteen Australian paleogeotherms derived from thermobarometric analysis of mantle xenoliths and xenocrysts (Supplementary Information). These come from a range of settings between thick and thin lithosphere. Localities with thin lithosphere tend to have data obtained from whole xenolith samples, typically hosted in basaltic volcanic products. For these cases, the compositions of multiple phases (garnet, clinopyroxene, orthopyroxene and olivine) can be obtained that all equilibrated under the same pressure-temperature (P-T) conditions. In these samples, we use a thermometer[39] that exploits exchange of calcium and magnesium between orthopyroxene and clinopyroxene and a barometer[40] based upon aluminium exchange between orthopyroxene and garnet, given by equation (5) of Nickel & Green (1985). This approach therefore requires compositions of garnet, diopside (clinopyroxene) and enstatite (orthopyroxene) for each xenolith. This barometer and thermometer pair both also depend upon the temperature and pressure, respectively. These two equations are therefore solved simultaneously by iteration to obtain equilibration P-T conditions. Samples are discarded if they fail more than one of the eight oxide, cation and equilibration checks.[41] Analyses from locations on thicker lithosphere are predominantly obtained from heavy mineral concentrates generated during diamond exploration (plus rare diamond inclusions and occasional whole peridotite xenoliths), where the association of one mineral grain with any other has been lost. Thus, the approach outlined above using multiple phases is unavailable, and we instead turn to single grain combined thermobarometers for deriving equilibration P-T conditions. For these samples, we use the chrome-in-diopside barometer[42] that exploits the exchange of chromium between clinopyroxene and garnet (Equation (9) of Nimis & Taylor, 2000). It uses only diopside compositions, but requires that garnet was also present in the source region. The associated thermometer[42] exploits enstatite-in-diopside, again using only diopside compositions but requiring that orthopyroxene was present within the source. The temperature is given by Equation (17) of Nimis & Taylor (2000). Again, these two equations must be solved by iteration to obtain P-T conditions for each diopside grain. Calibration on laboratory experiments has shown that this thermobarometer may become innacurate at low pressures and at temperatures <700°C.[41] We therefore only use P-T estimates derived from this thermobarometer that yield depths >60 km and pass both of the clinopyroxene cation and oxide checks.

Fitting a geotherm to P-T estimates. For each locality, P-T estimates derived from thermobarometry are entered into FITPLOT[43,44] to constrain the best-fitting paleogeotherm (Supplementary Information). Within the crust, we adopt a constant conductivity of 2.5 W m^{-1} °C^{-1}, whilst a pressure- and temperature-dependent parameterisation[45] is used within the mantle. Radiogenic heat production is assumed to be 1.12 μW m^{-3} in the upper crust, 0.40 μW m^{-3} in the lower crust and zero within the mantle.[46] Crustal thickness at each location is obtained from the AusMoho model[47], with upper and lower crustal layers assigned equal thicknesses. We assume a potential temperature of 1333°C, which is the temperature required to match the thickness and geochemistry of mid-ocean ridge basalt from a dry lherzolite source using a corner-flow melting parameterisation.[48,49] Self-consistent parameters are used to calculate the adiabatic gradient, including a reference density of $\rho_0 = 3.3$ Mg m^{-3}, thermal expansivity of $\alpha = 3 \times 10^{-5}$ °C^{-1} and specific heat capacity of $C_P = 1187$ J kg^{-1} °C^{-1}.

Calibrating V_S to temperature conversion. Anelasticity parameters A_B, α_B, τ'_P, $\beta(\phi_m)$, γ, T'_η and $\lambda\phi$ have been directly constrained by forced oscillation experiments on borneol.[15] However, μ^0_U, $\frac{\partial \mu_U}{\partial T}$, $\frac{\partial \mu_U}{\partial P}$, η_r, E_a, V_a and $T_S(z)$ must be independently determined by inverting real-Earth observational constraints on temperature, shear-wave velocity, attenuation and viscosity. Therefore, the SL2013sv global V_S model[17] is stacked in oceanic regions to calculate average V_S as a function of depth and lithospheric age. The age grid and optimal thermal model for a cooling oceanic plate are adopted from Richards et al. (2018).[18] At each depth slice of the tomography model, a suite of V_S versus temperature tie-points are extracted. Misfit, H_1, between predicted and observed V_S is

$$H_1 = \sqrt{\frac{1}{N}\sum_{i=1}^{N}\frac{1}{M}\sum_{j=1}^{M}\left(\frac{V^o_{ij} - V^c_{ij}}{\sigma_{ij}}\right)^2} \tag{16}$$

where V^o_{ij} are observed shear-wave velocities with associated standard deviation σ_{ij}, V^c_{ij} is the prediction from Equation (1), M is the number of age bins at a given depth and N is the number of depth slices. A second suite of tie-points is created by assuming that temperatures are isentropic at depths well below the upper thermal boundary layer. We calculate average V_S as a function of depth over oceanic regions in the global model, and over the whole spatial domain in regional models. Over the depth range 250–400 km, beyond which the resolving power of surface waves drops significantly, these values are combined with an isentrope calculated for pyrolite with a potential temperature of 1334 °C using Perple_X. Misfit for the isentrope, H_2, is

$$H_2 = \sqrt{\frac{1}{N}\sum_{i=1}^{N}\left(\frac{V^o_i - V^c_i}{\sigma_i}\right)^2} \tag{17}$$

It has been observed that over the depth range 150–400 km, both V_S and Q_S^{-1} are relatively consistent for oceanic ages $\geq$ 100 Ma. Over this range, we stack the QRFSI12 attenuation model[50], generating a suite of Q_S^{-1} to V_S tie-points as a function of depth. Equations (1) and (15) are coupled such that average temperature is obtained from the average V_S, rather than assuming isentropic temperatures extend up to 150 km. Misfit, H_3, between observed and predicted attenuation is

$$H_3 = \sqrt{\frac{1}{N}\sum_{i=1}^{N}\left(\frac{Q_i^{-1\ o} - Q_i^{-1\ c}}{\sigma_i^*}\right)^2} \tag{18}$$

We also adopt the bulk viscosity measurement[51] of $\eta_{ref} = 3 \times 10^{20}$ Pa s for upper mantle ($\sim$ 100–670 km) and compare it to the mean predicted value for 225–400 km depths obtained from Equation (7). Misfit, H_4, is calculated using

$$H_4 = \sqrt{\left(\left\{\frac{1}{N}\sum_{i=1}^{N}\log_{10}[\eta_i^c]\right\} - \log_{10}[\eta_{ref}]\right)^2} \tag{19}$$

where η_i^c is predicted viscosity. Finally, for calibration of regional tomography models, we take the better constrained paleogeotherms derived from thermobarometry on mantle xenoliths. Argyle, Boowinda Creek, Bullenmerri, Ellendale, Merline, Monaro, Monk Hill, Orroroo and Wandagee are used to constrain each anelasticity model. None of these paleogeotherms show evidence of having been perturbed by heating events immediately prior to xenolith entrainment therefore the calculated PT conditions are taken to indicate ambient mantle conditions at entrainment. Less well constrained paleogeotherms from Bow Hill, Cleve, Cone 32, Jugiong, Mt St Martin and Sapphire Hill are used to visually check results. For each utilised paleogeotherm we extract temperatures every 5 km between the base of the thermal boundary layer and either 125 km for regions with thick lithosphere, or 50 km for those with thin (<100 km) lithosphere. These variable top depths minimise the impact of potential crustal bleeding artefacts. Extracting $V_S(z)$ values at each paleogeotherm location yields a suite of V_S to temperature tie-points. Misfit, H_5, is calculated from

$$H_5 = \sqrt{\frac{1}{N}\sum_{i=1}^{N}\frac{1}{M}\sum_{j=1}^{M}\left(\frac{V_{ij}^o - V_{ij}^c}{\sigma_{ij}}\right)^2} \tag{20}$$

where M is the number of paleogeotherms, N is the number of tie-points associated with each geotherm and σ_{ij} reflects uncertainty in the V_S measurement, assumed to be a constant 0.1 km s^{-1} which captures typical variations between different tomography models at a given location. Combined misfit, H, is given by

$$H = \frac{w_1 H_1 + w_2 H_2 + w_3 H_3 + w_4 H_4 + w_5 H_5}{w_1 + w_2 + w_3 + w_4 + w_5} \tag{21}$$

where w represents weighting applied to each misfit constraint. H is minimised in two steps. Initially, a parameter sweep is performed to identify the approximate location of the global minimum. μ_U^0 is varied between 69–82 GPa (in increments of 1 GPa), $\frac{\partial\mu}{\partial T}$ between -20 and -8 MPa °C^{-1} (2 MPa °C^{-1} increments), $\frac{\partial\mu}{\partial T}$ between 1.5–2.9 (0.2 increments), η_r between 10^{17}–10^{23} Pa s ($10^{0.5}$ Pa s increments), E_a between 100–1000 kJ mol^{-1} (100 kJ mol^{-1} increments), V_a between 0–30 cm^3 mol^{-1} (2 cm^3 mol^{-1} increments) and $\frac{\partial T_s}{\partial z}$ between 0–4.5 °C km^{-1} (0.25 °C km^{-1} increments), in line with ranges of previous estimates obtained from laboratory experiments and other studies.[14,15,52] Secondly, Powell's conjugate gradient algorithm is used to further minimise H using best-fitting parameters from the initial sweep as the starting point. For calibration of the global model SL2013sv, we set $w_1 = 10$, $w_2 = 1$, $w_3 = 2$, $w_4 = 2$ and $w_5 = 0$, which yields a minimum misfit $H = 0.682$ when $\mu_U^0 = 76.3$ GPa,

$\frac{\partial \mu_U}{\partial T} = -17.7$ MPa °C^{-1}, $\frac{\partial \mu_U}{\partial P} = 2.53$, $\eta_r = 1.23 \times 10^{21}$ Pa s, $E_a = 202$ kJ mol^{-1}, $V_a = 1.92$ cm^3 mol^{-1} and $\frac{\partial T_s}{\partial z} = 0.955$ °C km^{-1}. These parameters are used to convert the full three-dimensional V_S model to temperature. For the regional model FR12 we constrain the calibration using the paleogeotherms. All weights are set to zero except for $w_2 = 1$ and $w_5 = 10$, yielding minimum misfit $H = 0.578$ when $\mu_U^0 = 69.3$ GPa, $\frac{\partial \mu_U}{\partial T} = -12.3$ MPa °C^{-1}, $\frac{\partial \mu_U}{\partial P} = 2.89$, $\eta_r = 1.93 \times 10^{22}$ Pa s, $E_a = 1000$ kJ mol^{-1}, $V_a = 0$ cm^3 mol^{-1} and $\frac{\partial T_s}{\partial z} = 4.50$ °C km^{-1}.

Mapping the lithosphere-asthenosphere boundary. A recent study[18] on the thermal structure of oceanic lithosphere found that the 1175 ± 50°C isotherm provides a good match to seismological observations of the lithosphere-asthenosphere boundary (LAB), such as peak variation in the orientation of azimuthal anisotropy. In this study, we therefore adopt this isotherm as a proxy for lithospheric thickness beneath the continents. $T(z)$ is extracted from the V_S model and $\frac{\partial T}{\partial z}$ calculated over 25 km increments. Starting from the surface and progressing downwards, when temperature passes the 1175°C threshold, LAB depth is calculated using linear interpolation, with one important exception. In locations of thick crust, low V_S values at shallow depths arising from crustal bleeding are erroneously interpreted as hot lithospheric mantle. In the regional seismic tomography models, this crustal bleeding can be observed down to $\sim$ 125 km in some locations (Figure S7). Therefore, when an inverted temperature gradient is found at shallow depths, we move on to deeper levels until temperature starts to increase with depth. This crustal bleeding is only considered down to 200 km. Maximum LAB depth is limited to 350 km or the deepest slice in the seismic tomography model. Our 1175°C isotherm LAB proxy is shallower than used in some other studies[44,14] that define the LAB using the intersection of conductive and adiabatic temperature gradients in the thermal boundary layer (typically occurring at temperatures 1350–1450°C). However, in addition to matching oceanic observations, the 1175°C isotherm corresponds to lower homologous temperatures, where uncertainty in anelasticity parameters has a smaller impact on the recovered LAB.

Test suites of random continental locations. In order to test the statistical significance of real deposit locations, a test suite of random points on a sphere have been generated by randomly selecting two variables, a and b, in the range 0–1 and converting into longitude, θ, and latitude, ϕ, using area-normalised relationships

$$\theta = 360 \times a \tag{22}$$

$$\phi = \frac{180}{\pi} \times \arcsin(2b - 1) \tag{23}$$

These are subsequently filtered to select only those points that lie onshore (Supplementary Information). For each location, the closest approach of the 170 km lithospheric thickness contour is calculated and the resulting distances are plotted in a cumulative distribution function (CDF).

Kolmogorov-Smirnov statistical tests. We use the *two-sample Kolmogorov-Smirnov test* to examine whether the difference between two cumulative distribution functions is significant, given their respective population sizes. The D-value is the maximum magnitude of the difference between two CDFs at any point.[20] The test calculates the probability that a D-value of this magnitude might accidentally occur, had the two CDFs been randomly selected from the same underlying population. The probability, P, is approximated using

$$P \approx \exp\left(\frac{-2pqD^2}{p+q}\right) \tag{24}$$

where p and q are the number of samples in each CDF and D is the D-value expressed as a fraction between 0 and 1. For each Kolmogorov-Smirnov test, a number of random points are generated that is equivalent to the number of real deposits of that type (109 for PbZn-CD, 147 for PbZn-MVT and 139 for sedimentary copper). Given the low sample size for some of the deposit classes, the distribution of this random set can vary somewhat from the true average distribution of random continental locations. We therefore draw a test set in this manner 100 times and report the Kolmogorov-Smirnov statistics associated with each separate test within a histogram. The D-value between the real non-weighted, regionally enhanced PbZn-CD CDF and each random CDF is individually calculated, yielding a mean and standard deviation of 0.36 ± 0.04 with extremes of 0.27–0.45. The equivalent values are 0.27 ± 0.02 with extremes of 0.23–0.32 for the combined sediment-hosted deposits in Figure 2. A D-value of 0.27 for the 395 combined sedimentary-hosted deposits suggests that the probability this CDF is drawn from randomly distributed continental points is less than 1 in 10^{12} (Supplementary Information).

References

[1] Ali, S. H. *et al.* Mineral supply for sustainable development requires resource governance. *Nature* **543**, 367–372 (2017).

[2] Schodde, R. Long term trends in global exploration – are we finding enough metal? In *11th Fennoscandian Exploration and Mining Conference, 31st October 2017* (Levi, Finland, 2017). URL `minexconsulting.com/publications/oct2017b`.

[3] Nassar, N. T., Graedel, T. E. & Harper, E. M. By-product metals are technologically essential but have problematic supply. *Science Advances* **1**, 1–11 (2015).

[4] McCuaig, T. C., Beresford, S. & Hronsky, J. Translating the mineral systems approach into an effective exploration targeting system. *Ore Geology Reviews* **38**, 128–138 (2010).

[5] Wyborn, L. A. I., Heinrich, C. A. & Jaques, A. L. Australian Proterozoic mineral systems: essential ingredients and mappable criteria. *Australian Institute of Mining and Metallurgy Annual Conference* 109–115 (1994).

[6] McCuaig, T. C. & Hronsky, J. M. A. The mineral system concept: The key to exploration targeting. In *Society of Economic Geologists Special Publication 18*, 153–175 (Society of Economic Geologists, 2014).

[7] Begg, G. C. *et al.* Lithospheric, cratonic, and geodynamic setting of Ni-Cu-PGE sulfide deposits. *Economic Geology* **105**, 1057–1070 (2010).

[8] Griffin, W. L., Begg, G. C. & O'Reilly, S. Y. Continental-root control on the genesis of magmatic ore deposits. *Nature Geoscience* **6**, 905–910 (2013).

[9] Leach, D. L. *et al.* Sediment-hosted lead-zinc deposits in Earth history. *Economic Geology* **105**, 593–625 (2010).

[10] Hitzman, M. W., Selley, D. & Bull, S. Formation of sedimentary rock-hosted stratiform copper deposits through Earth history. *Economic Geology* **105**, 627–639 (2010).

[11] Huston, D. L. *et al.* Tectono-metallogenic systems – The place of mineral systems within tectonic evolution, with an emphasis on Australian examples. *Ore Geology Reviews* **76**, 168–210 (2016).

[12] McCuaig, T. C., Scarselli, S., O'Connor, T., Busuttil, S. & N, M. The Power of a Systems Approach to Mineral and Petroleum Exploration in Sedimentary Basins. *SEG Special Publication* **21** (2018).

[13] Geophysical Archive Data Delivery System (GADDS) (2018). URL `geoscience.gov.au/gadds`.

[14] Priestley, K. & McKenzie, D. P. The relationship between shear wave velocity, temperature, attenuation and viscosity in the shallow part of the mantle. *Earth and Planetary Science Letters* **381**, 78–91 (2013).

[15] Yamauchi, H. & Takei, Y. Polycrystal anelasticity at near-solidus temperatures. *Journal of Geophysical Research: Solid Earth* **121**, 7790–7820 (2016).

[16] Fishwick, S. & Rawlinson, N. 3-D structure of the Australian lithosphere from evolving seismic datasets. *Australian Journal of Earth Sciences* **59**, 809–826 (2012).

[17] Schaeffer, A. J. & Lebedev, S. Global shear speed structure of the upper mantle and transition zone. *Geophysical Journal International* **194**, 417–449 (2013).

[18] Richards, F. D., Hoggard, M. J., Cowton, L. R. & White, N. J. Reassessing the thermal structure of oceanic lithosphere with revised global inventories of basement depths and heat flow measurements. *Journal of Geophysical Research: Solid Earth* **123**, 9136–9161 (2018).

[19] Huston, D. L. & Champion, D. C. Spatial variations in lead isotope ratios from the Mount Isa–McArthur mineral province, northeast Australia: Evidence for a cryptic crustal margin controlling the distribution of world-class sediment-hosted zinc-lead-silver deposits .

[20] Kolmogorov, A. N. Sulla determinazione empirica di una legge di distribuzione. *Giornale dell'Istituto Italiano degli Attuari* **4**, 83–91 (1933).

[21] Menzies, M., Xu, Y., Zhang, H. & Fan, W. Integration of geology, geophysics and geochemistry: A key to understanding the North China Craton. *Lithos* **96**, 1–21 (2007).

[22] Manning, A. H. & Emsbo, P. Testing the potential role of brine reflux in the formation of sedimentary exhalative (sedex) ore deposits. *Ore Geology Reviews* **102**, 862–874 (2018).

[23] Sloan, R. A., Jackson, J. A., McKenzie, D. P. & Priestley, K. Earthquake depth distributions in central Asia, and their relations with lithosphere thickness, shortening and extension. *Geophysical Journal International* **185**, 1–29 (2011).

[24] Gibson, G. *et al.* Basin architecture and evolution in the mount isa mineral province, northern australia: Constraints from deep seismic reflection profiling and implications for ore genesis. *Ore Geology Reviews* **76**, 414 – 441 (2016). URL `http://www.sciencedirect.com/science/article/pii/S0169136815002036`.

[25] Davies, D. R. & Rawlinson, N. On the origin of recent intraplate volcanism in Australia. *Geology* **42**, 1031–1034 (2014).

[26] Huston, D. L., Pehrsson, S., Eglington, B. M. & Zaw, K. The geology and metallogeny of volcanic-hosted massive sulfide deposits: Variations through geologic time and with tectonic setting. *Economic Geology* **105**, 571–591 (2010).

[27] Arndt, N. T., Lesher, C. M. & Czamanske, G. K. Mantle-derived magmas and magmatic Ni-Cu-(PGE) deposits. *Economic Geology 100th Anniversary Volume* 5–24 (2005).

[28] Raymond, O. Australian Geological Provinces 2018.01 edition. *Geoscience Australia Dataset* **eCat Id: 1** (2018). URL `ecat.ga.gov.au/geonetwork`.

[29] Hitzman, M. W., Kirkham, R., Broughton, D., Thorson, J. & Selley, D. The sediment-hosted stratiform Copper ore system. *Economic Geology 100th Anniversary Volume* (2005).

[30] Cox, D. P., Lindsey, D. A., Singer, D. A., Moring, B. C. & Diggles, M. F. Sediment-hosted copper deposits of the world: Deposit models and database. *U.S. Geological Survey Open-File Report* (2007).

[31] Taylor, R. D., Leach, D. L., Bradley, D. C. & Pisarevsky, S. A. Compilation of mineral resource data for Mississippi Valley-type and clastic-dominated sediment-hosted lead-zinc deposits. *U.S. Geological Survey Open-File Report* **1297** (2009).

[32] Sillitoe, R. H. Porphyry copper systems. *Economic Geology* **105**, 3–41 (2010).

[33] Hoatson, D. M., Jaireth, S. & Jaques, A. L. Nickel sulfide deposits in Australia: Characteristics, resources, and potential. *Ore Geology Reviews* **29**, 177–241 (2006).

[34] Franklin, J. M., Gibson, H. L., Jonasson, I. R. & Galley, A. G. Volcanogenic massive sulfide deposits. *Economic Geology 100th Anniversary Volume* (2005).

[35] Sexton, J. Australian mineral occurrences collection. *Geoscience Australia Dataset* **eCat Id 73** (2011). URL `ecat.ga.gov.au/geonetwork`.

[36] Fishwick, S., Heintz, M., Kennett, B. L. N., Reading, A. M. & Yoshizawa, K. Steps in lithospheric thickness within eastern Australia, evidence from surface wave tomography. *Tectonics* **27** (2008).

[37] Hirschmann, M. M. Mantle solidus: Experimental constraints and the effects of peridotite composition. *Geochemistry Geophysics Geosystems* **1** (2000).

[38] Grose, C. J. & Afonso, J. C. Comprehensive plate models for the thermal evolution of oceanic lithosphere. *Geochemistry, Geophysics, Geosystems* **14** (2013).

[39] Taylor, W. R. An experimental test of some geothermometer and geobarometer formulations for upper mantle peridotites with application to the thermobarometry of fertile lherzolite and garnet websterite. *Neues Jahrbuch für Mineralogie - Abhandlungen* **172**, 381–408 (1998).

[40] Nickel, K. G. & Green, D. H. Empirical geothermobarometry for garnet peridotites and implications for the nature of the lithosphere, kimberlites and diamonds. *Earth and Planetary Science Letters* **73**, 158–170 (1985).

[41] Nimis, P. & Grütter, H. Internally consistent geothermometers for garnet peridotites and pyroxenites. *Contributions to Mineralogy and Petrology* **159**, 411–427 (2010).

[42] Nimis, P. & Taylor, W. R. Single clinopyroxene thermobarometry for garnet peridotites. Part I. Calibration and testing of a Cr-in-Cpx barometer and an enstatite-in-Cpx thermometer. *Contributions to Mineralogy and Petrology* **139**, 541–554 (2000).

[43] McKenzie, D. P., Jackson, J. & Priestley, K. Thermal structure of oceanic and continental lithosphere. *Earth and Planetary Science Letters* **233**, 337–349 (2005).

[44] Mather, K. A., Pearson, D. G., McKenzie, D. P., Kjarsgaard, B. A. & Priestley, K. Constraints on the depth and thermal history of cratonic lithosphere from peridotite xenoliths, xenocrysts and seismology. *Lithos* **125**, 729–742 (2011).

[45] Osako, M., Ito, E. & Yoneda, A. Simultaneous measurements of thermal conductivity and thermal diffusivity for garnet and olivine under high pressure. *Physics of the Earth and Planetary Interiors* **143-144**, 311–320 (2004).

[46] Jaupart, C., Labrosse, S. & Mareschal, J. C. Temperatures, Heat and Energy in the Mantle of the Earth. *Treatise on Geophysics* **7**, 253–303 (2007).

[47] Kennett, B. L. N., Salmon, M., Saygin, E. & Group, A. W. AusMoho: The variation of Moho depth in Australia. *Geophysical Journal International* **187**, 946–958 (2011).

[48] Katz, R. F., Spiegelman, M. & Langmuir, C. H. A new parameterization of hydrous mantle melting. *Geochemistry, Geophysics, Geosystems* **4** (2003).

[49] Shorttle, O., Maclennan, J. & Lambart, S. Quantifying lithological variability in the mantle. *Earth and Planetary Science Letters* **395**, 24–40 (2014).

[50] Dalton, C. A., Ekström, G. & Dziewonski, A. M. Global seismological shear velocity and attenuation: A comparison with experimental observations. *Earth and Planetary Science Letters* **284**, 65–75 (2009).

[51] Lau, H. C. *et al.* Inferences of mantle viscosity based on ice age data sets: Radial structure. *Journal of Geophysical Research: Solid Earth* **121**, 6991–7012 (2016).

[52] Jain, C., Korenaga, J. & Karato, S. I. On the grain size sensitivity of olivine rheology. *Journal of Geophysical Research: Solid Earth* **123**, 674–688 (2018).

[53] Kennett, B. L. N., Fichtner, A., Fishwick, S. & Yoshizawa, K. Australian seismological reference model (AuSREM): Mantle component. *Geophysical Journal International* **192**, 871–887 (2013).

[54] Yoshizawa, K. & Kennett, B. L. N. Multimode surface wave tomography for the Australian region using a three-stage approach incorporating finite frequency effects. *Journal of Geophysical Research: Solid Earth* **109**, 1–19 (2004).

[55] Fichtner, A., Kennett, B. L. N., Igel, H. & Bunge, H.-P. Full waveform tomography for radially anisotropic structure: New insights into present and past states of the Australasian upper mantle. *Earth and Planetary Science Letters* **290**, 270–280 (2010).

[56] Fichtner, A., Igel, H., Bunge, H.-P. & Kennett, B. L. N. Simulation and inversion of seismic wave propagation on continental scales based on a spectral-element method. *Journal of Numerical Analysis, Industrial and Applied Mathematics* **4**, 11–22 (2009).

[57] Fichtner, A., Kennett, B. L. N., Igel, H. & Bunge, H.-P. Full seismic waveform tomography for upper-mantle structure in the Australasian region using adjoint methods. *Geophysical Journal International* **179**, 1703–1725 (2009).

[58] Yoshizawa, K. Radially anisotropic 3-D shear wave structure of the Australian lithosphere and asthenosphere from multi-mode surface waves. *Physics of the Earth and Planetary Interiors* **235**, 33–48 (2014).

[59] Davies, D. R., Rawlinson, N., Iaffaldano, G. & Campbell, I. H. Lithospheric controls on magma composition along Earth's longest continental hotspot track. *Nature* **525**, 511–514 (2015).

[60] Czarnota, K., Roberts, G. G., White, N. J. & Fishwick, S. Spatial and temporal patterns of Australian dynamic topography from river profile modeling. *Journal of Geophysical Research: Solid Earth* **119**, 1384–1424 (2014).

[61] Artemieva, I. M. Global 1 1 thermal model TC1 for the continental lithosphere: Implications for lithosphere secular evolution. *Tectonophysics* **416**, 245–277 (2006).

[62] Bird, P., Liu, Z. & Rucker, W. K. Stresses that drive the plates from below: Definitions, computational path, model optimization, and error analysis. *Journal of Geophysical Research: Solid Earth* **113** (2008).

[63] Steinberger, B. & Becker, T. W. A comparison of lithospheric thickness models. *Tectonophysics* 1–14 (2016).

[64] Pasyanos, M. E., Masters, T. G., Laske, G. & Ma, Z. LITHO1.0: An updated crust and lithospheric model of the Earth. *Journal of Geophysical Research: Solid Earth* **119**, 2153–2173 (2014).

Acknowledgments: We are grateful to B. Steinberger, N. Rawlinson, K. Yoshizawa and B. Kennett for sharing lithospheric thickness maps. We thank J.C. Afonso, J. Austermann, G. Begg, R. Blewett, A. Bufe, D. Champion, R. Davies, B. Delbridge, M. Doublier, R. Fu, S. Goes, A. Gorbatov, B. Hodgin, B. Holtzman, J. Kingslake, T. Mackey, D. McKenzie, J. Mitrovica, D. Müller, P. Nimis, E. Powell, K. Priestley, D. Schutt, O. Shorttle, R. Skirrow, S. Stephenson, Y. Takei & J. Winterbourne for their assistance and discussions. This work is a contribution to the Australian Government's Exploring for the Future program. KC and DH publish with the permission of the CEO of Geoscience Australia. MH acknowledges support from the National Aeronautics and Space Administration grant NNX17AE17G and the American Chemical Society Petroleum Research Fund 59062-DNI8. FR acknowledges support from the Schmidt Science Fellows program, in partnership with the Rhodes Trust.

Author contributions: This study was conceived by KC. KC and DH compiled deposit databases. LJ collated Australian xenolith data. Thermobarometry was done by LJ, FR and MH. Paleogeotherm modelling was done by FR and LJ. FR and MH developed shear-wave to temperature conversion scheme. FR calibrated anelasticity parameterisations. MH generated LAB maps, performed statistical tests, made figures and compiled supplementary materials. The paper was written by KC and MH, with guidance from all authors.

Competing interests: The authors declare no competing financial interests.

Data availability: All data is available in the manuscript or the supplementary materials. Correspondence should be addressed to K. Czarnota (karol.czarnota@ga.gov.au) and M. Hoggard (mark_hoggard@fas.harvard.edu).

Supplementary Information:

- Additional Materials
- Figures S1–S20
- References (54–64)

Supplementary Information for "Gigayear stability of cratonic edges controls global distribution of sediment-hosted metals"

Karol Czarnota[*,1,2], Mark J. Hoggard[*,3,4], Fred D. Richards[3], David L. Huston[1] & A. Lynton Jaques[2]

1. Geoscience Australia, GPO Box 378, Canberra ACT 2601, Australia.
2. Research School of Earth Sciences, Australian National University, Canberra, ACT 0200, Australia
3. Department of Earth & Planetary Sciences, Harvard University, 20 Oxford Street, Cambridge, MA 02138, USA.
4. Lamont-Doherty Earth Observatory, Columbia University, 61 Rte 9W, Palisades, NY 10964, USA.

*karol.czarnota@ga.gov.au; mark_hoggard@fas.harvard.edu

Contents

Additional Supporting Information (Files uploaded separately)

1. Global and Australian lithospheric thickness maps in ASCII format.
2. Database of six major classes of base metal deposit.
3. Location and diopside compositions for xenocryst thermobarometry.
4. Fifteen Australian FITPLOT geotherms in ASCII format.

Seismic Tomography Model Comparison

Our LAB maps are based on the most recent, high-resolution shear wave tomography models. For the global map, we use SL2013sv[17] which is an upper mantle-only model built from a combination of body and surface waves, including fundamental and higher modes. Periods considered are 11–450 s, $\sim 750,000$ seismograms are included, and misfits are calculated between synthetics and the full waveform up to the 9^{th} overtone. Crucially, simultaneous inversion for the crustal model results in minimal smearing of slow crustal velocities down into the upper mantle, thereby allowing us to use more depth slices in our V_S to temperature calibration. Checkerboard resolution tests indicate that features ~ 600 km in diameter at lithospheric depths are generally well resolved. Finer features should be resolvable in regions with dense ray path coverage, such as North America, Europe and southeast Asia.

The SL2013sv model contains only 6 seismometers in Australia, so has limited resolution within this continent. Therefore, we also investigate three regional seismic tomography models to generate high resolution maps for the Australian continent. The main model used throughout this paper is the radially isotropic V_S model FR12[16], which is derived from Rayleigh wave travel times.[36] Periods considered are 50–120 s and the fundamental and first four higher modes have been used where possible, leading to good sensitivity down to ~ 250 km depths. It contains a greater number of source–receiver paths ($> 13,000$) compared to other Australian models. However, it uses an *a priori* crustal model that remains fixed throughout the inversion, resulting in noticeable smearing of crustal velocities into the upper mantle. Checkerboard tests indicate that features ~ 300 km in diameter at lithospheric depths are well resolved.

The second regional model is AuSREM[53] and is a hybrid model constructed by linear combination of several previous studies. It combines FR12 with YK04[54] and AMSAN.19.[55] YK04 is a radially anisotropic Rayleigh wave model using > 8000 ray paths for the fundamental mode and ~ 2000 for the first three higher modes, yielding a maximum period range of 40–150 s. It includes off-great circle and finite frequency effects, but also uses a fixed crustal model. AMSAN.19 is a radially anisotropic, 3D waveform, spectral element model that uses an inversion scheme based on the adjoint approach.[56,57] Periods considered are 30–200 s and a fixed crustal model is used. Due to the computationally intensive methodology, $\sim 3,000$ waveforms are used in this inversion.

The third and final regional model considered in this study is the radially anisotropic Y14.[58] It combines Rayleigh waves (8000 fundamental, ~ 2500 higher mode) and Love waves (approximately two-thirds as many) with periods $\sim$ 25–200s, corrected for local crustal structure using a fixed crustal model. It adopts the same three-step inversion procedure as YK04.[54] All three models are plotted alongside the global SL2013sv model in Figures S1, S2 and S3. At any given location within the continent, V_S varies between models by ~ 0.1 km s^{-1}.

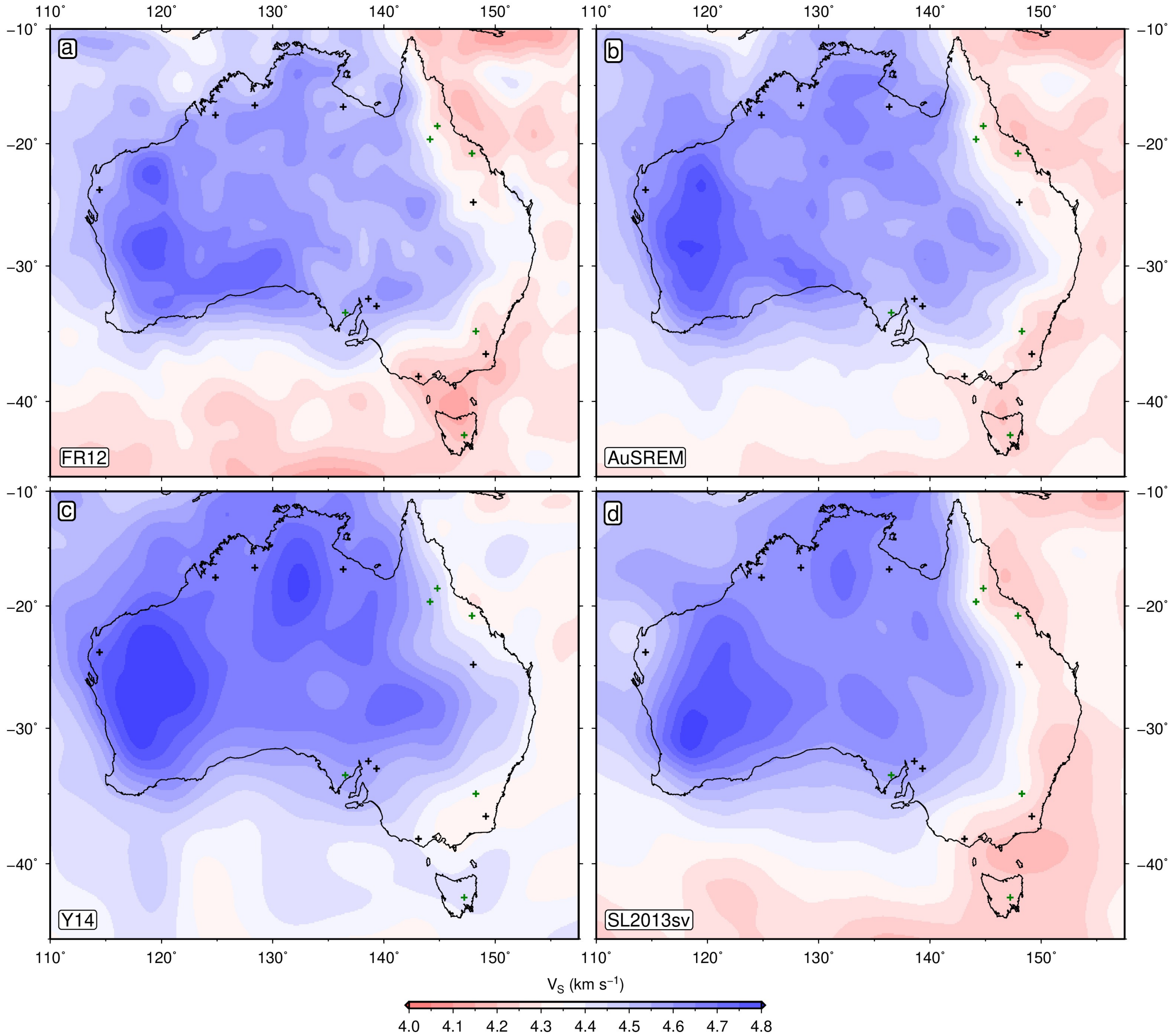

Figure S1: **100 km depth slice through Australian seismic tomography models.** Black/green crosses = paleogeotherms used as constraints/tests in anelasticity calibration. (a) FR12 = regional isotropic V_S [16]. (b) AuSREM = regional V_{SV} [53]. (c) Y14 = regional V_{SV} [58]. (d) SL2013sv = global V_{SV} [17].

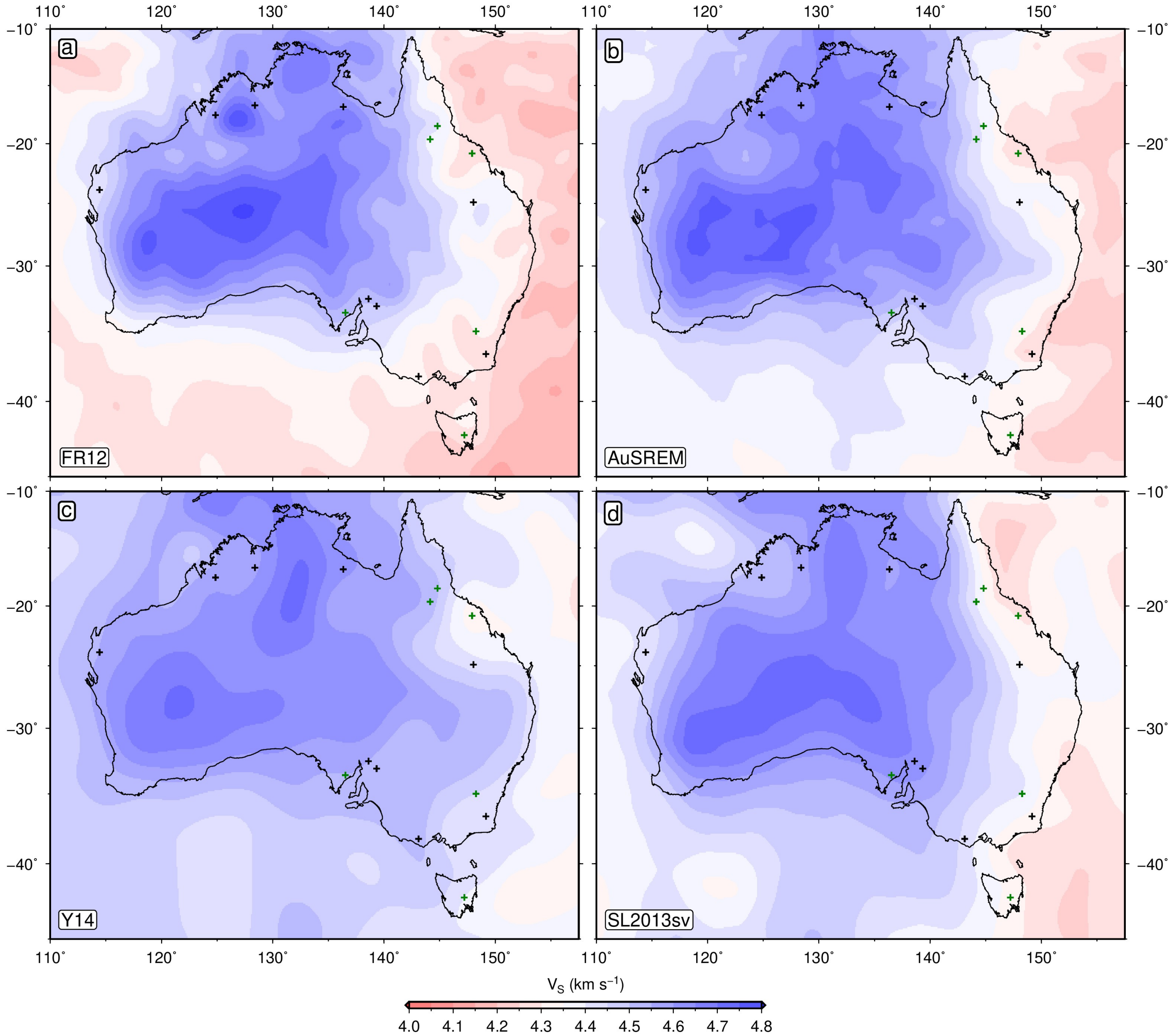

Figure S2: **175 km depth slice through Australian seismic tomography models.** Black/green crosses = paleogeotherms used as constraints/tests in anelasticity calibration. (a) FR12 = regional isotropic V_S [16]. (b) AuSREM = regional V_{SV} [53]. (c) Y14 = regional V_{SV} [58]. (d) SL2013sv = global V_{SV} [17].

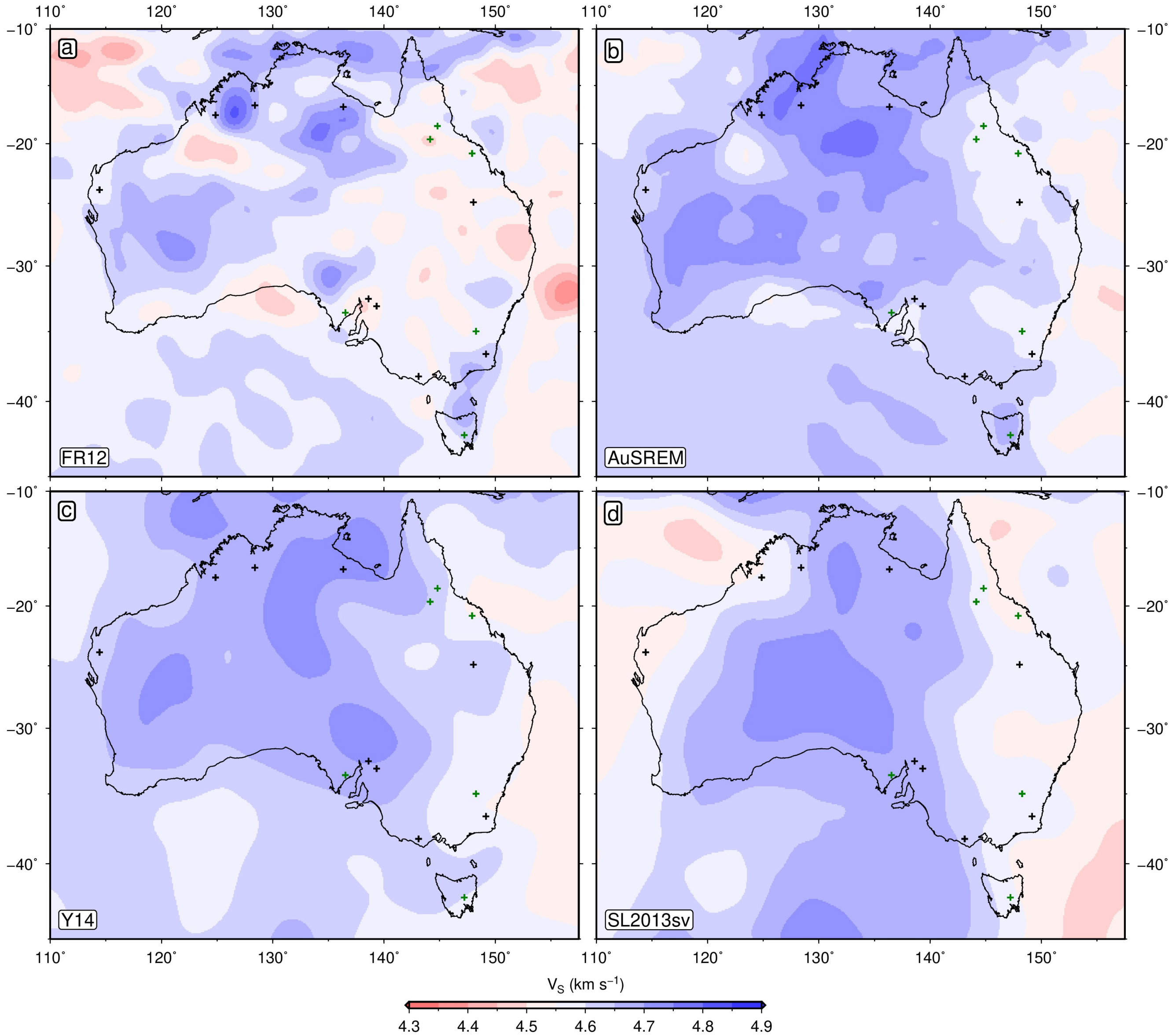

Figure S3: **250 km depth slice through Australian seismic tomography models.** Black/green crosses = paleogeotherms used as constraints/tests in anelasticity calibration. (a) FR12 = regional isotropic V_S [16]. (b) AuSREM = regional V_{SV} [53]. (c) Y14 = regional V_{SV} [58]. (d) SL2013sv = global V_{SV} [17].

Thermobarometry and Regional Calibration of Tomography Models

Temperature estimates across a range of depths are required to generate a series of V_S-T-P tie points in order to calibrate the regional seismic tomography models. We therefore assemble a suite of Australian paleogeotherms derived from thermobarometric analysis of mantle xenoliths and xenocrysts from fifteen locations in thick and thin lithosphere (Figure S4). The resulting P-T estimates are entered into FITPLOT to generate the palaeogeotherms shown in Figure S5 (Methods).

The results of regional calibration using the paleogeotherms are shown in Figures S6 and S7. Note that the global model SL2013sv yields good fits to paleogeotherms away from south Australia (Monk Hill, Orroroo and Cleve), despite being lower resolution than the local models and being calibrated completely independently of this information (red lines in Figure S7). Conversely, regional models often provide a poorer fit to the full range of the paleogeotherms and can exhibit substantial crustal bleeding artefacts at depths shallower than ~ 125 km. Generally amongst the regional models, FR12 performs the best, followed by AuSREM and then Y14.

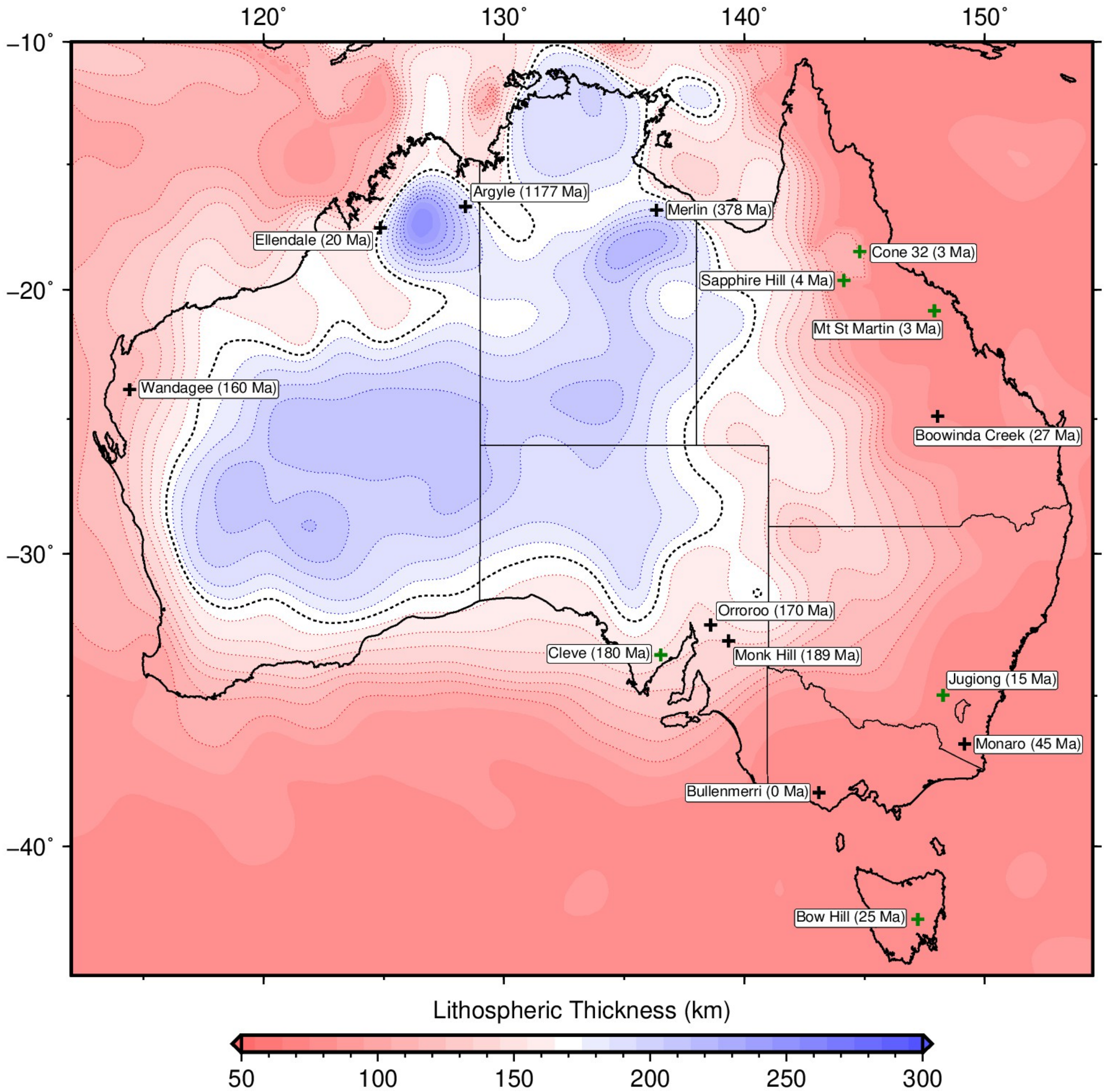

Figure S4: **Location of Australian xenolith and xenocryst suites.** Labels give site name and age (in million years); black crosses = locations used to constrain anelasticity calibration, green crosses = locations used to visually test validity of results; red/blue colours = lithospheric thickness (from Figure 1b), derived from FR12 seismic tomography model.[16]

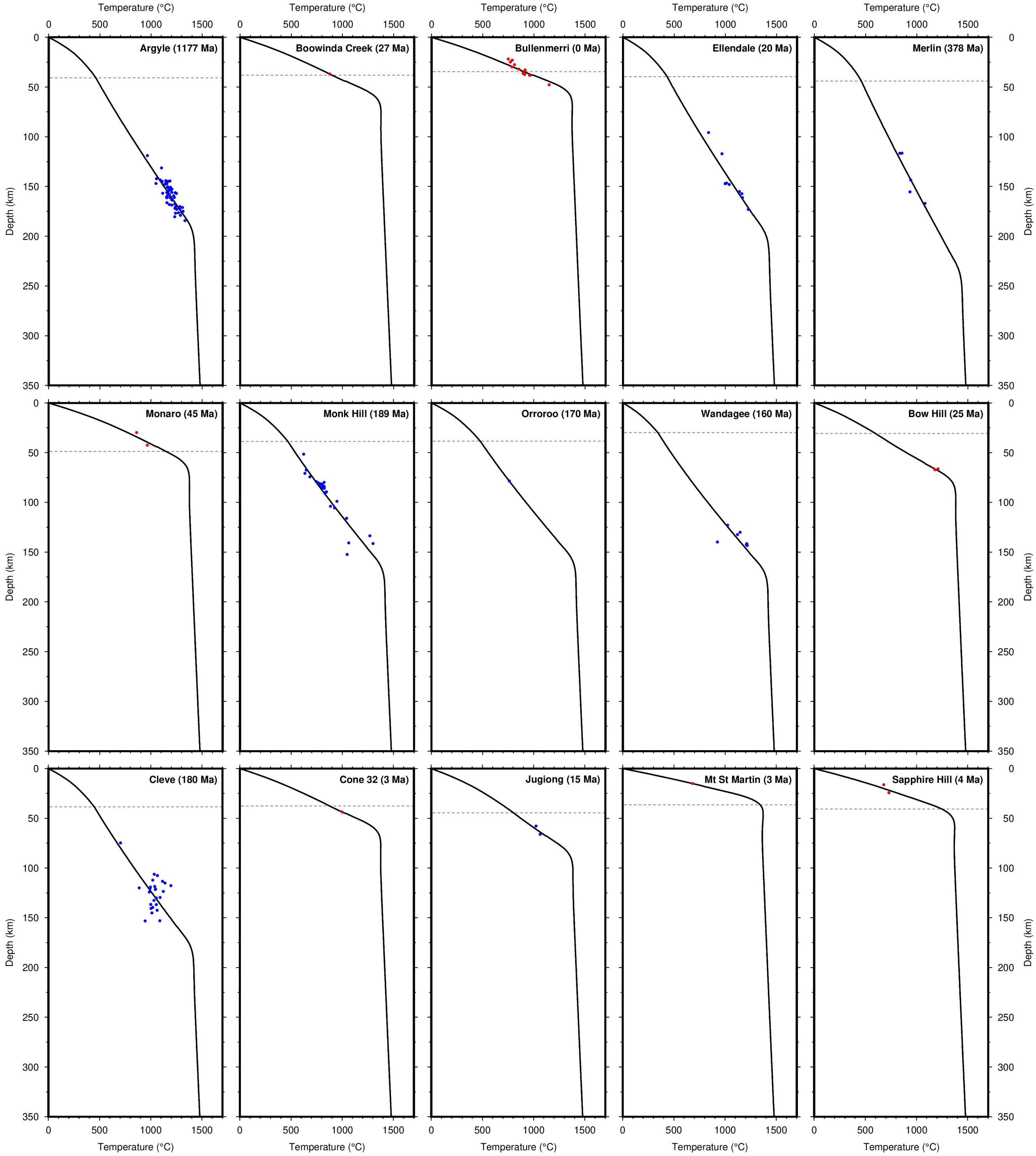

Figure S5: **Australian paleogeotherms derived from xenolith and xenocryst thermobarometry.** Labels give site name and age (in million years) from Figure S4; red circles = P-T estimates derived from multiphase thermobarometry[40,39]; blue circles = P-T estimates derived from single chrome diopside thermobarometry[42]; dashed line = crustal thickness from AusMoho[47]; solid line = FITPLOT optimal paleogeotherm.

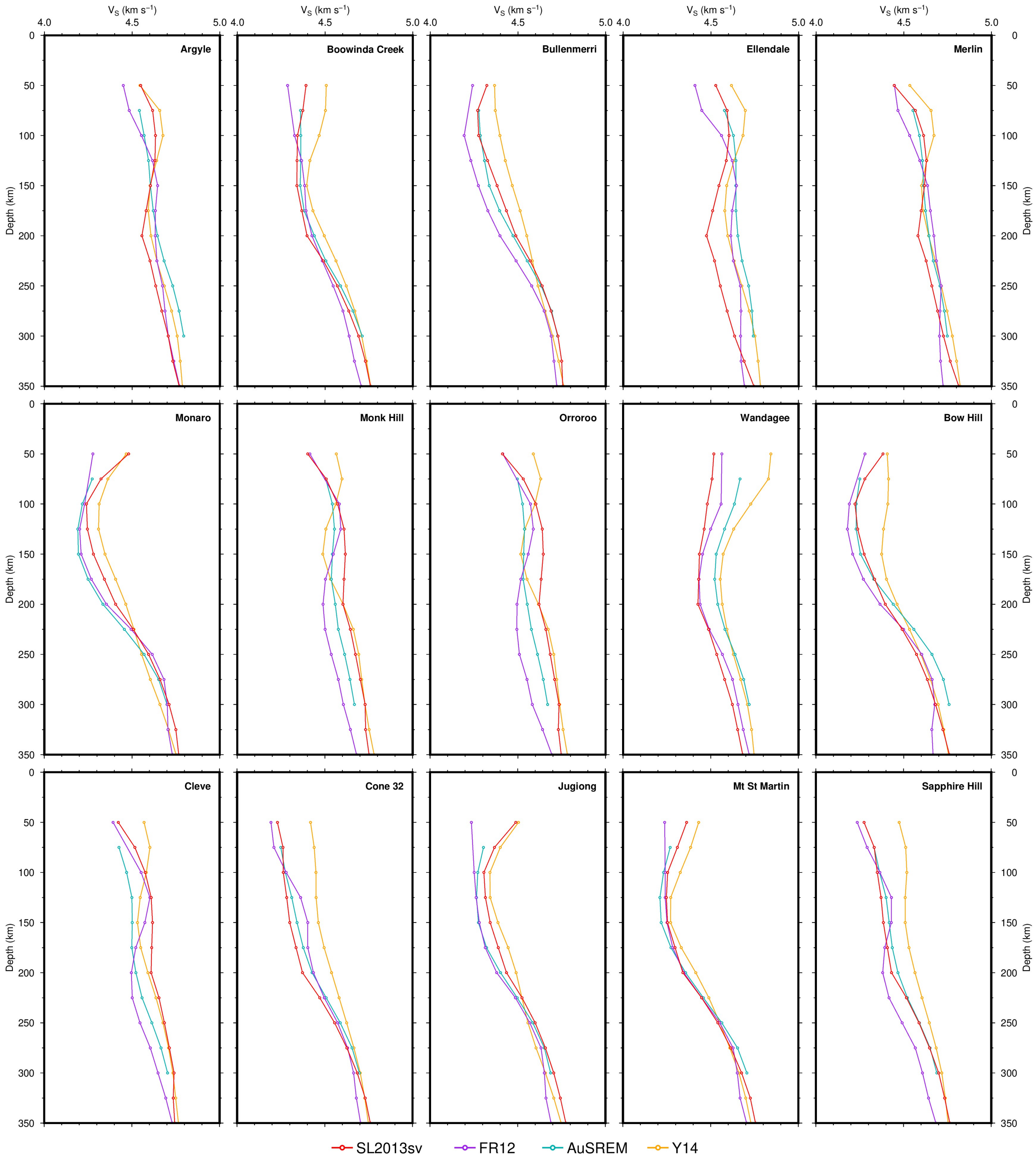

Figure S6: **V_S as a function of depth at sites of fifteen Australian paleogeotherms.** Labels give site name (locations in Figure S4); red = global SL2013sv model[17]; purple = regional FR12 model[16]; blue = regional AuSREM model[53]; orange = regional Y14 model[58].

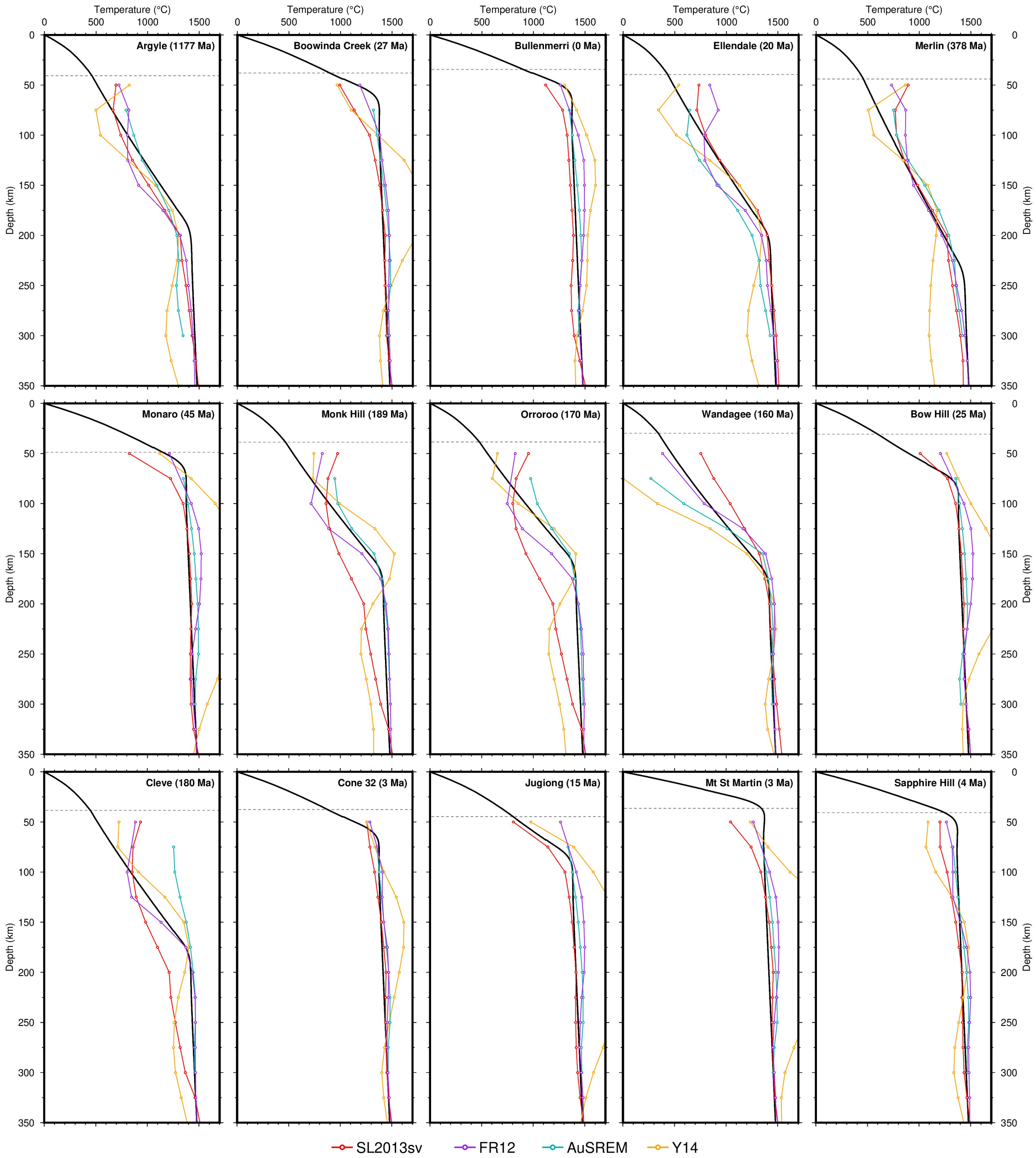

Figure S7: **Calibration of anelasticity parameterisation on Australian paleogeotherms.** Labels give site name and inferred age of paleogeotherms in million years (locations in Figure S4); sites Argyle to Wandagee are used to constrain calibration; sites Bow Hill to Sapphire Hill are used to visually check output; dashed line = crustal thickness from AusMoho[47]; solid line = optimal FITPLOT geotherm from Figure S5; purple = regional FR12 model[16]; blue = regional AuSREM model[53]; orange = regional Y14 model[58]; red = global SL2013sv model[17], for comparison, calibrated independently of palaeogeotherm constraints.

Australian Lithospheric Thickness Maps

For each of the individually calibrated seismic tomography models in this study, we have mapped out the LAB in a consistent manner. The resulting maps for Australia are shown in Figure S8, whilst in Figure S9 we compare our preferred FR12 regional model to previously published maps of LAB depth beneath Australia.

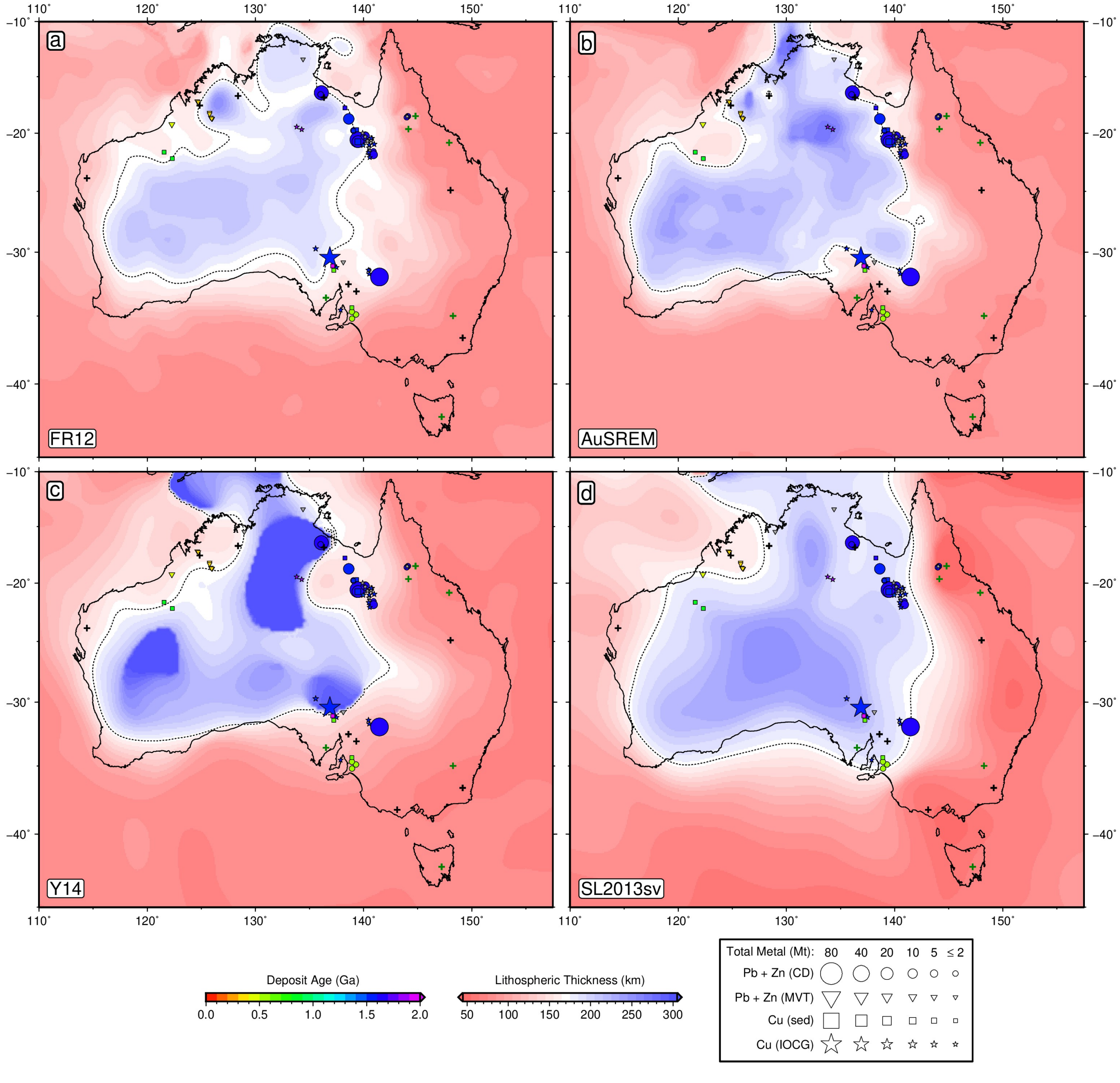

Figure S8: **Depth to lithosphere-asthenosphere boundary from individually calibrated Australian seismic tomography models.** Black contour = 170 km LAB thickness; green/black crosses = paleogeotherms used/unused in anelasticity calibration; other symbols = sediment-hosted deposit locations; area proportional to estimate of total contained mass of metal (MT = megatonnes); unknown deposit size given 2 Mt symbol; colour = ore body formation age (billion years); unknown age plotted in grey; circles = clastic-dominated lead-zinc (PbZn-CD); triangles = Mississippi Valley type lead-zinc (PbZn-MVT); squares = sedimentary copper (Cu-sed); stars = iron-oxide-copper-gold (IOCG). (a) based on FR12.[16] (b) based on AuSREM.[53] (c) based on Y14.[58] (d) based on global SL2013sv.[17]

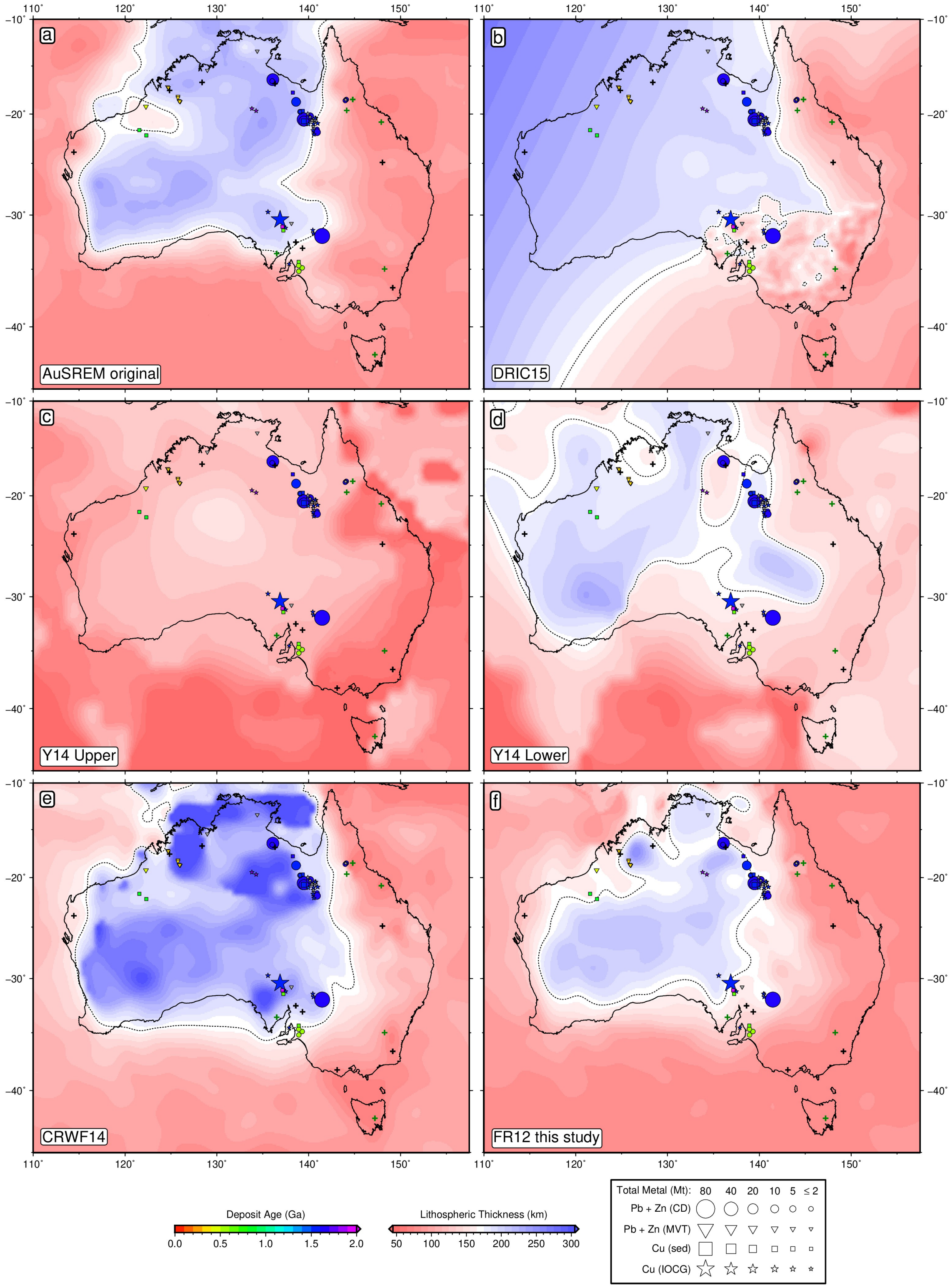

Figure S9: **Depth to lithosphere-asthenosphere boundary beneath Australia from previous studies.** Black contour = 170 km LAB thickness; green/white crosses = paleogeotherms used/unused in anelasticity calibration; other symbols = sediment-hosted deposit locations; area proportional to estimate of total contained mass of metal (MT = megatonnes); unknown deposit size given 2 Mt symbol; colour = ore body formation age (billion years); unknown age plotted in grey; circles = clastic-dominated lead-zinc (PbZn-CD); triangles = Mississippi Valley type lead-zinc (PbZn-MVT); squares = sedimentary copper (Cu-sed); stars = iron-oxide-copper-gold (IOCG). (a) Original AuSREM.[53] (b) DRIC15.[59] (c) Upper bound of Y14.[58] (d) Lower bound of Y14.[58] (e) CRWF14[60], derived using FR12 tomography.[16] (f) FR12 LAB model generated in this study.

Histogram of Global Lithospheric Thickness

Global LAB thickness derived from the SL2013sv model[17] reveals a bi-modal population with peaks at 80 km and 180 km, separated by a minimum at 150 km (Figure S10). There is also a noticeable drop-off deeper than 200 km, which we attribute to a change in the gradient of V_S with depth in the initial starting profile used to construct the tomography model.

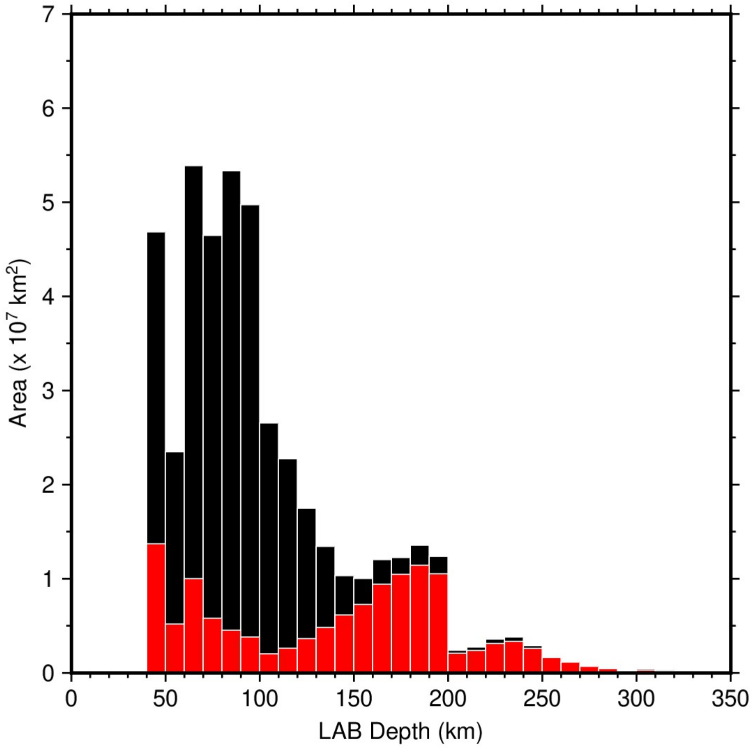

Figure S10: **Area-weighted histogram of global LAB depths.** LAB derived from the SL2013sv tomography model[17]; black bars = oceanic regions; red bars = continental regions.

Previously Published Global LAB Maps

For comparison, we provide five previously published global lithosphere-asthenosphere boundary (LAB) maps derived from a mixture of heat flow data and seismic tomography datasets. Interestingly, many giant sediment hosted mineral deposits lie along LAB edges defined by these other studies, testifying to the veracity of the observed relationship.

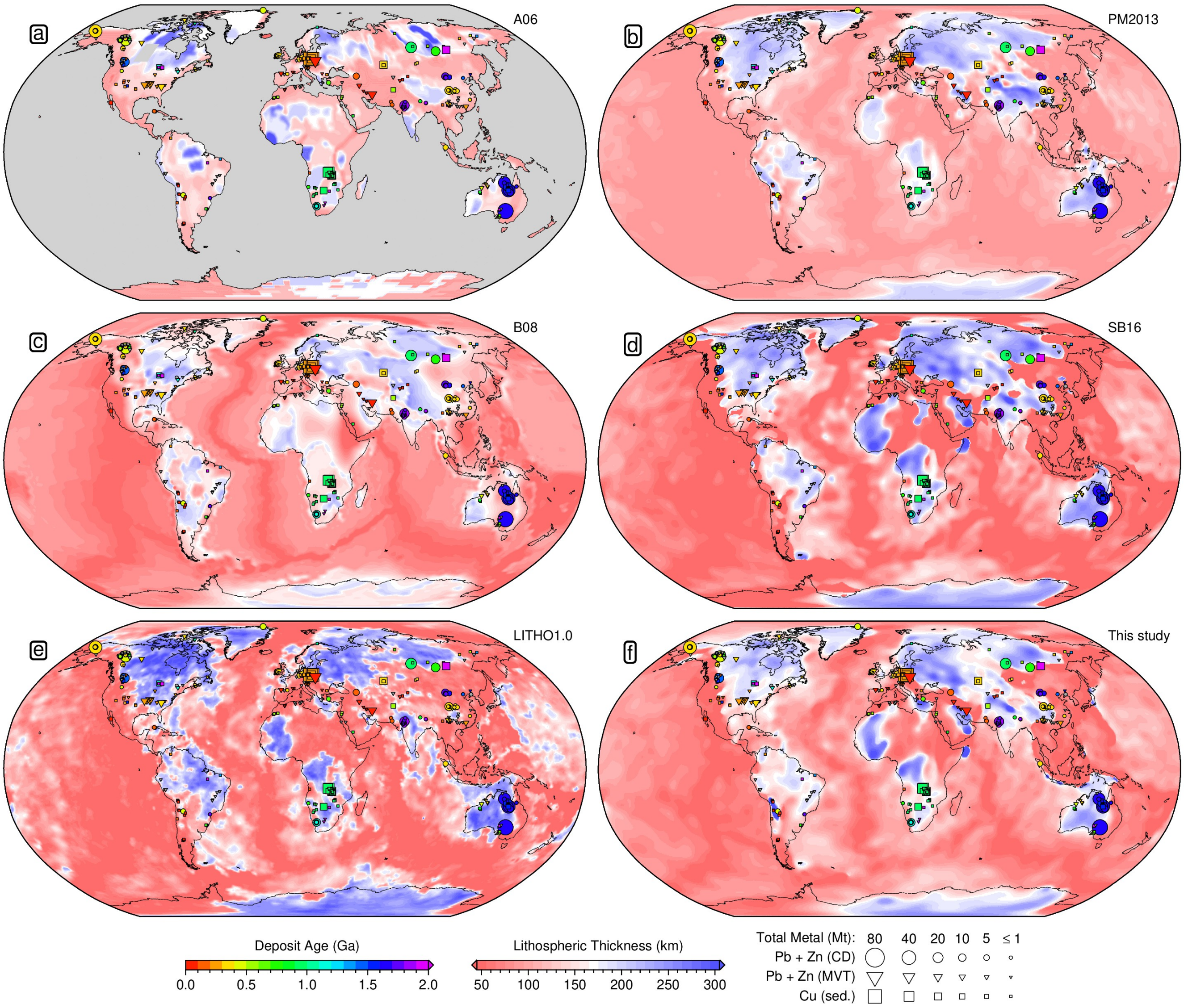

Figure S11: **Previously published global maps of depth to the lithosphere-asthenosphere boundary.** Symbols = sediment-hosted deposit locations; area proportional to estimate of total contained mass of metal (MT = megatonnes); unknown deposit size given 1 Mt symbol; colour = ore body formation age (billion years); unknown age plotted in grey; circles = clastic-dominated lead-zinc (PbZn-CD); triangles = Mississippi Valley type lead-zinc (PbZn-MVT); squares = sedimentary copper (Cu-sed). (a) LAB derived from surface heat flow measurements[61]; (b) LAB derived from surface wave tomography[14]; (c) LAB derived from vertical shear-wave travel time anomalies in the continents[62]; (d) LAB[63] derived from SL2013sv tomography model[17]; (e) LAB derived from surface wave tomography[64]; (f) LAB derived in this study using SL2013sv tomography model[17].

Kolmogorov-Smirnov Statistical Tests

In order to test the statistical significance of real deposit locations, test suites of random points on a sphere are generated. Example test suites of 100, 1000 and 10,000 points are shown in Figure S12.

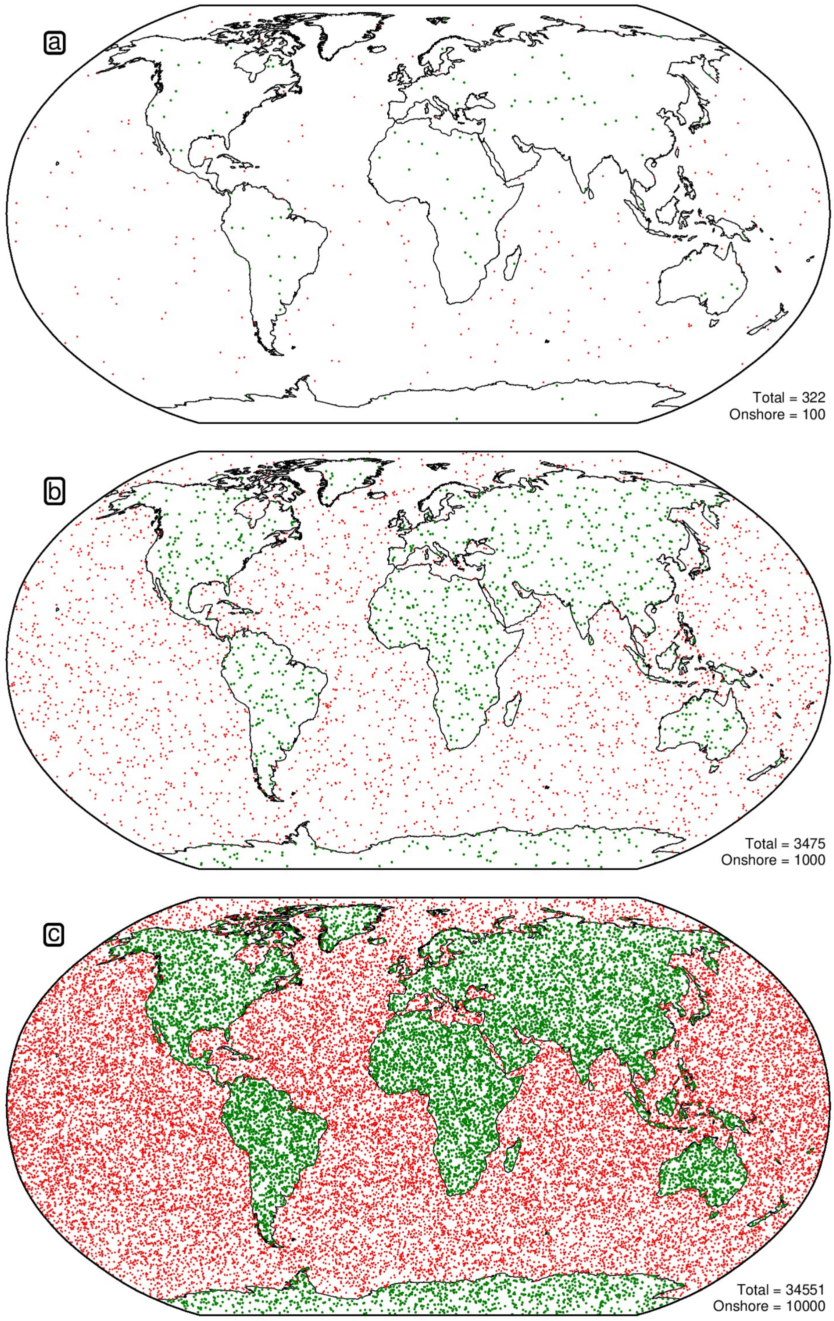

Figure S12: **Distribution of random points on the surface of a sphere.** Green circles = onshore points; red = offshore. (a) Example set of 100 onshore points. (b) Example set of 1000 onshore points. (c) Example set of 10,000 onshore points.

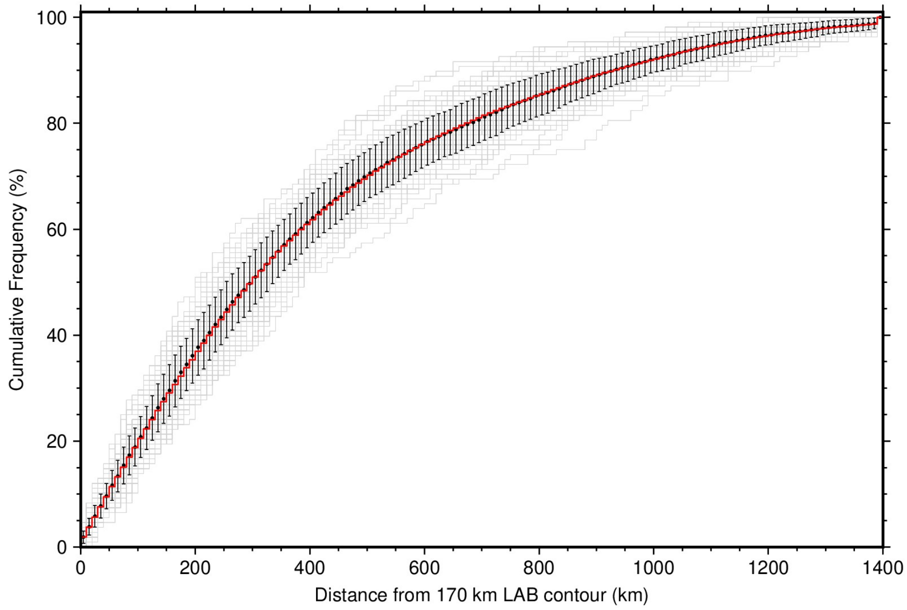

Figure S13: **Cumulative distribution functions for random continental points with distance from the 170 km LAB thickness contour.** Grey lines = 100 CDFs for a set of 109 random points in the continents; black points with error bars = mean and standard deviation of all 100 CDFs within each 10 km bin; red line = CDF for a set of 10,000 random continental points.

For each Kolmogorov-Smirnov test, a number of random points are generated that is equivalent to the number of real deposits of that type (109 for PbZn-CD, 147 for PbZn-MVT and 139 for sedimentary copper). Given the low sample size for some of the deposit classes, the distribution of this random set can vary somewhat from the true average distribution of continental locations. We therefore draw a test set in this manner 100 times (Figure S13). These random CDFs are relatively consistent but have some outliers. The D-value and Kolmogorov-Smirnov statistics between each random CDF and the real one is calculated and reported within a histogram (Figure S14).

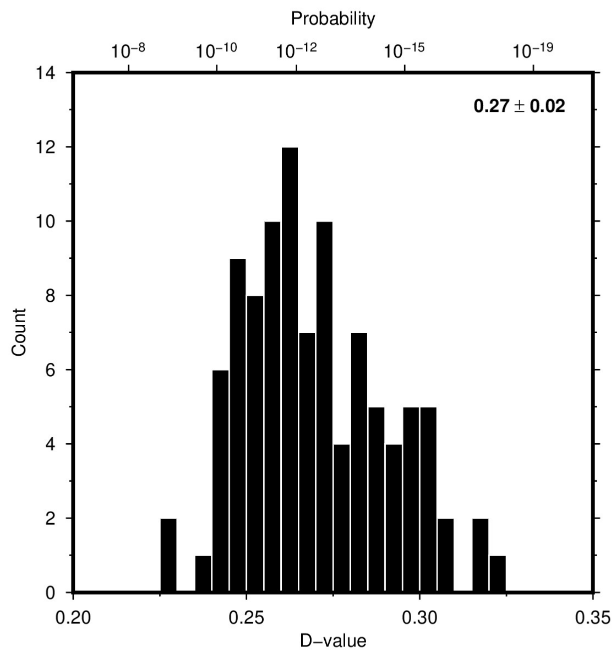

Figure S14: **D-values for all 395 sediment-hosted base metal deposits.** Histogram of D-values for ensemble of 100 random CDFs calculated for each random test set compared with the non-mass-weighted, locally enhanced CDF; inset lists mean and standard deviation of D-values; associated probabilities shown across top.

Deposit Compilation

Figures S15–S20 show deposit locations, age distributions with respect to LAB thickness, and Kolmogorov-Smirnov statistical test results for each individual deposit type.

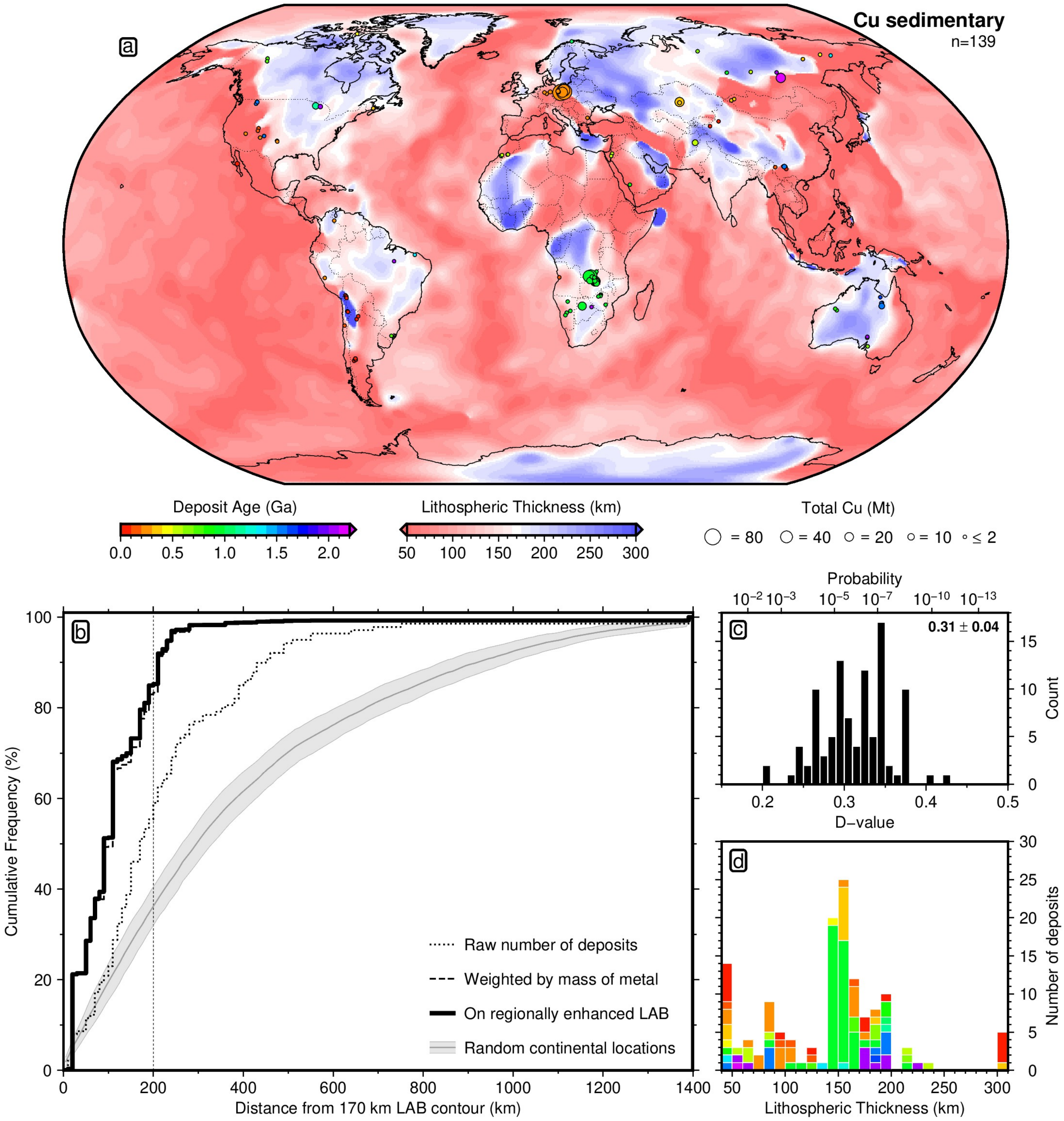

Figure S15: **139 sedimentary copper deposits.** (a) LAB derived from SL2013sv tomography model using a calibrated anelasticity parameterisation.[17,15] Circles = deposit locations; area proportional to estimate of total contained mass of metal (MT = megatonnes); unknown deposit size given 2 Mt symbol; colour = ore body formation age (billion years); unknown age plotted in grey. (b) Different approaches for generating cumulative distribution functions. Dotted line = simple count of number of deposits with increasing distance from the 170 km contour in global LAB map; dashed line = weighting by contained mass of copper; solid black line = mass of metal-weighted deposits where Australian LAB has been replaced with regionally enhanced map (Figure S8a); grey line/bounds = mean and standard deviation of 100 sets of equivalent number of randomly drawn continental locations, with respect to regionally enhanced LAB. (c) Histogram of 100 D-values calculated for each random test set and a non-mass-weighted, locally enhanced CDF; inset lists mean and standard deviation of D-values; associated probabilities shown across top. (d) Histogram of deposit occurrence as a function of lithospheric thickness, coloured by deposit age.

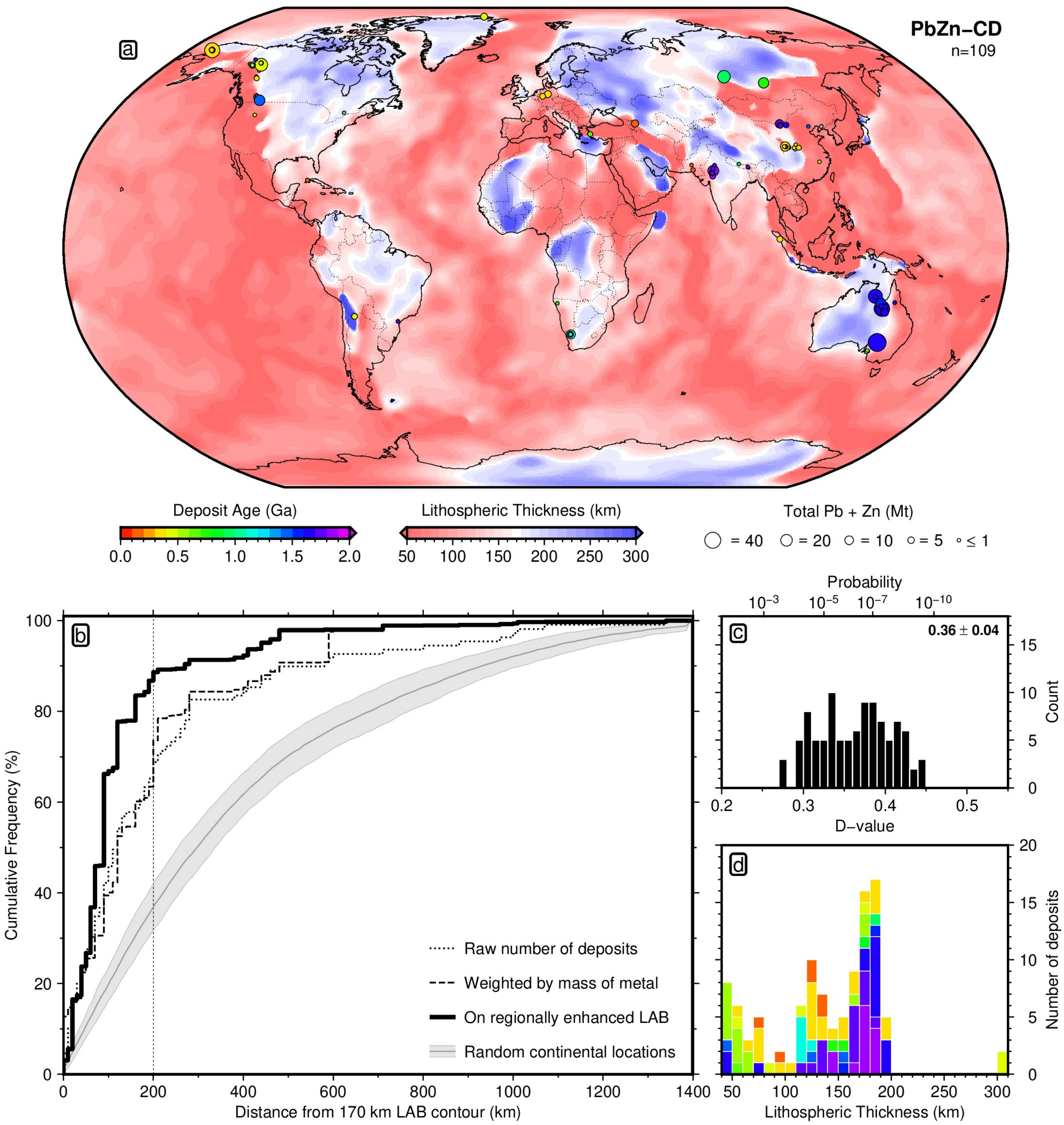

Figure S16: **109 clastic-dominated lead-zinc deposits.** (a) LAB derived from SL2013sv tomography model using a calibrated anelasticity parameterisation.[17,15] Circles = deposit locations; area proportional to estimate of total contained mass of metal (MT = megatonnes); unknown deposit size given 1 Mt symbol; colour = ore body formation age (billion years); unknown age plotted in grey. (b) Different approaches for generating cumulative distribution functions. Dotted line = simple count of number of deposits with increasing distance from the 170 km contour in global LAB map; dashed line = weighting by contained mass of lead and zinc; solid black line = mass of metal-weighted deposits where Australian LAB has been replaced with regionally enhanced map (Figure S8a); grey line/bounds = mean and standard deviation of 100 sets of equivalent number of randomly drawn continental locations, with respect to regionally enhanced LAB. (c) Histogram of 100 D-values calculated for each random test set and a non-mass-weighted, locally enhanced CDF; inset lists mean and standard deviation of D-values; associated probabilities shown across top. (d) Histogram of deposit occurrence as a function of lithospheric thickness, coloured by deposit age.

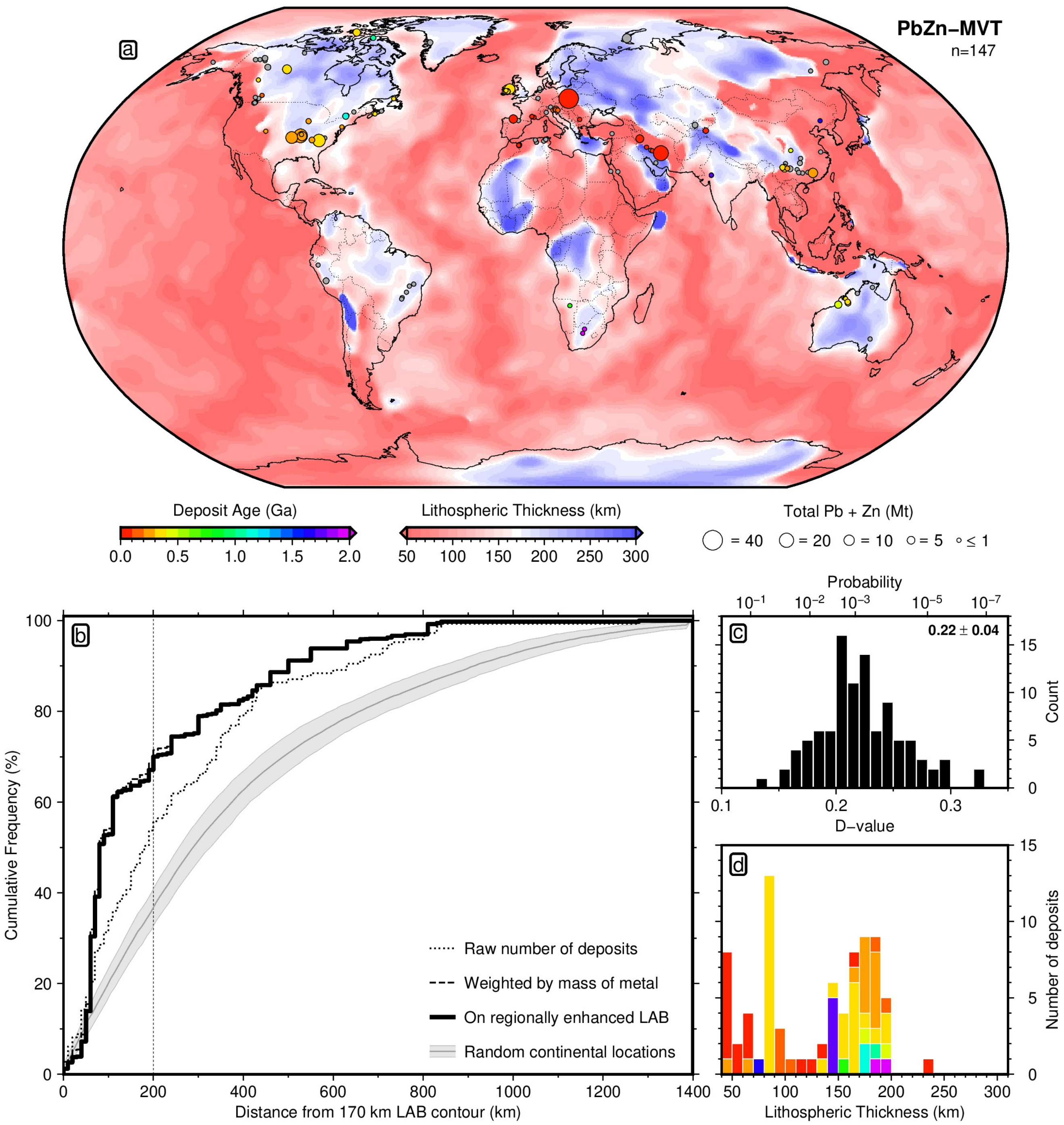

Figure S17: **147 Mississippi Valley-type lead-zinc deposits.** (a) LAB derived from SL2013sv tomography model using a calibrated anelasticity parameterisation.[17,15] Circles = deposit locations; area proportional to estimate of total contained mass of metal (MT = megatonnes); unknown deposit size given 1 Mt symbol; colour = ore body formation age (billion years); unknown age plotted in grey. (b) Different approaches for generating cumulative distribution functions. Dotted line = simple count of number of deposits with increasing distance from the 170 km contour in global LAB map; dashed line = weighting by contained mass of lead and zinc; solid black line = mass of metal-weighted deposits where Australian LAB has been replaced with regionally enhanced map (Figure S8a); grey line/bounds = mean and standard deviation of 100 sets of equivalent number of randomly drawn continental locations, with respect to regionally enhanced LAB. (c) Histogram of 100 D-values calculated for each random test set and a non-mass-weighted, locally enhanced CDF; inset lists mean and standard deviation of D-values; associated probabilities shown across top. (d) Histogram of deposit occurrence as a function of lithospheric thickness, coloured by deposit age.

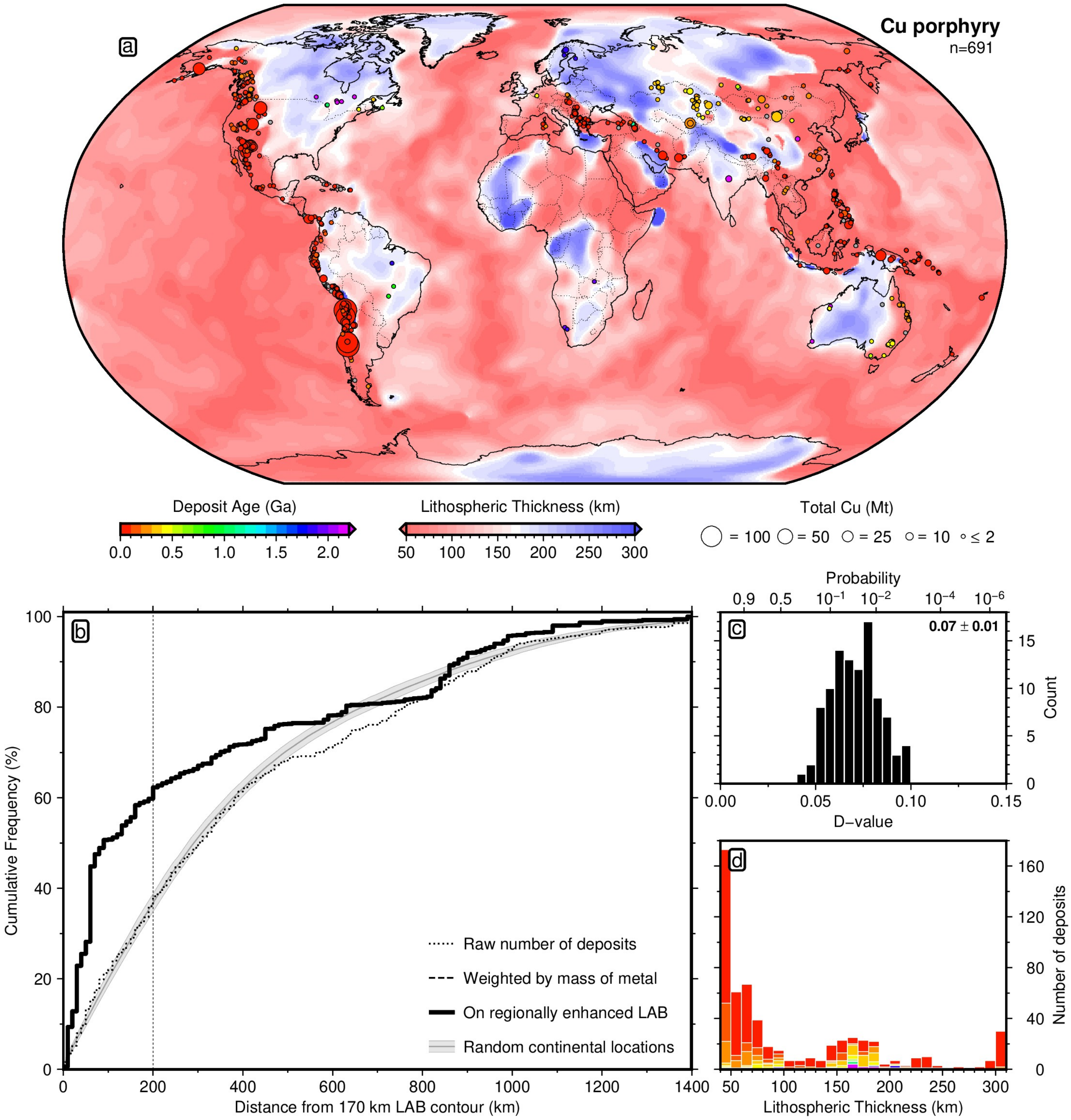

Figure S18: **691 copper porphyry deposits.** (a) LAB derived from SL2013sv tomography model using a calibrated anelasticity parameterisation.[17,15] Circles = deposit locations; area proportional to estimate of total contained mass of metal (MT = megatonnes); unknown deposit size given 2 Mt symbol; colour = ore body formation age (billion years); unknown age plotted in grey. (b) Different approaches for generating cumulative distribution functions. Dotted line = simple count of number of deposits with increasing distance from the 170 km contour in global LAB map; dashed line = weighting by contained mass of copper; solid black line = mass of metal-weighted deposits where Australian LAB has been replaced with regionally enhanced map (Figure S8a); grey line/bounds = mean and standard deviation of 100 sets of equivalent number of randomly drawn continental locations, with respect to regionally enhanced LAB. (c) Histogram of 100 D-values calculated for each random test set and the a non-mass-weighted, locally enhanced CDF; inset lists mean and standard deviation of D-values; associated probabilities shown across top. (d) Histogram of deposit occurrence as a function of lithospheric thickness, coloured by deposit age.

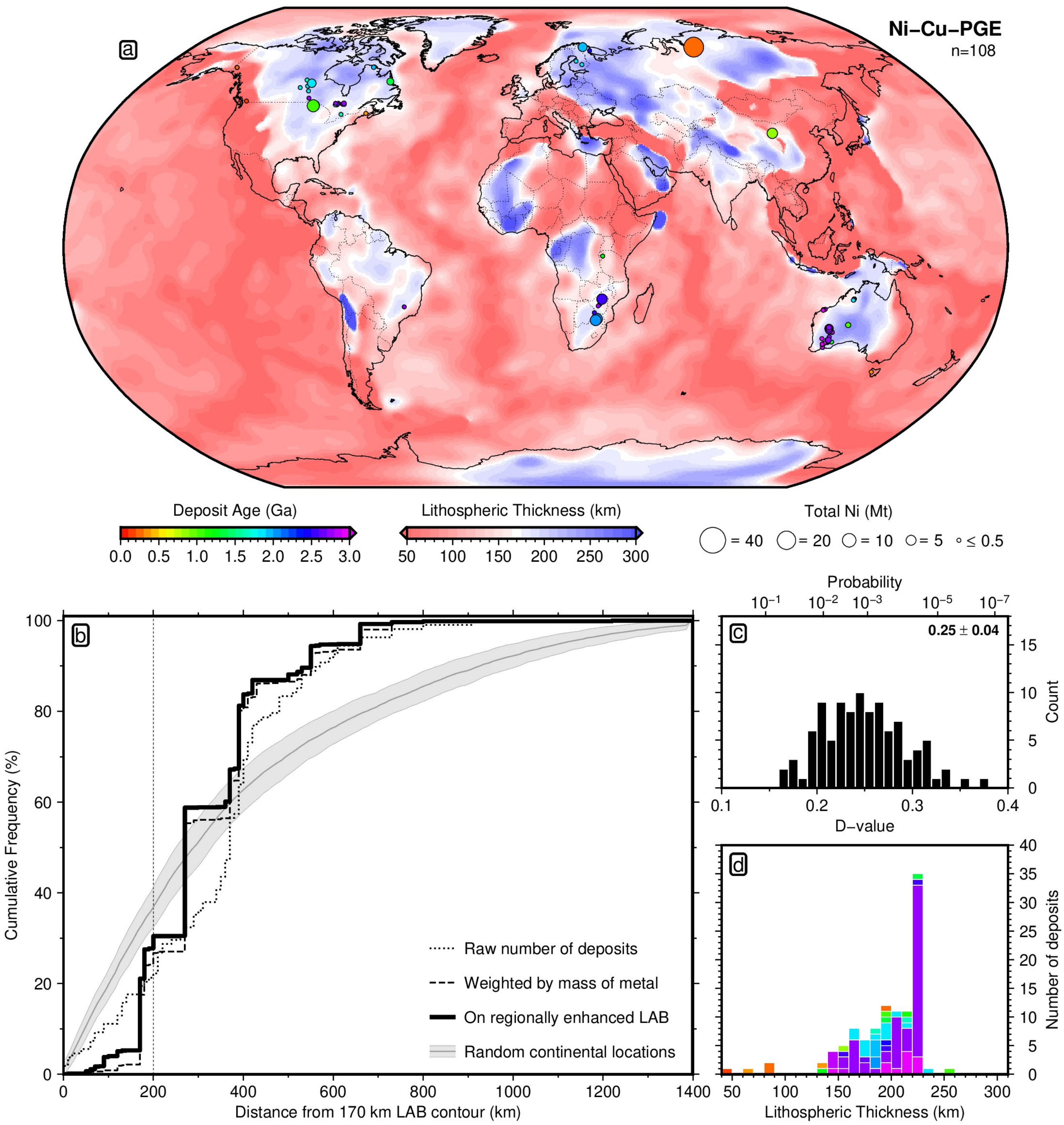

Figure S19: **108 magmatic nickel-copper-platinum group element deposits.** (a) LAB derived from SL2013sv tomography model using a calibrated anelasticity parameterisation.[17,15] Circles = deposit locations; area proportional to estimate of total contained mass of metal (MT = megatonnes); unknown deposit size given 0.5 Mt symbol; colour = ore body formation age (billion years); unknown age plotted in grey. (b) Different approaches for generating cumulative distribution functions. Dotted line = simple count of number of deposits with increasing distance from the 170 km contour in global LAB map; dashed line = weighting by contained mass of nickel; solid black line = mass of metal-weighted deposits where Australian LAB has been replaced with regionally enhanced map (Figure S8a); grey line/bounds = mean and standard deviation of 100 sets of equivalent number of randomly drawn continental locations, with respect to regionally enhanced LAB. (c) Histogram of 100 D-values calculated for each random test set and a non-mass-weighted, locally enhanced CDF; inset lists mean and standard deviation of D-values; associated probabilities shown across top. (d) Histogram of deposit occurrence as a function of lithospheric thickness, coloured by deposit age.

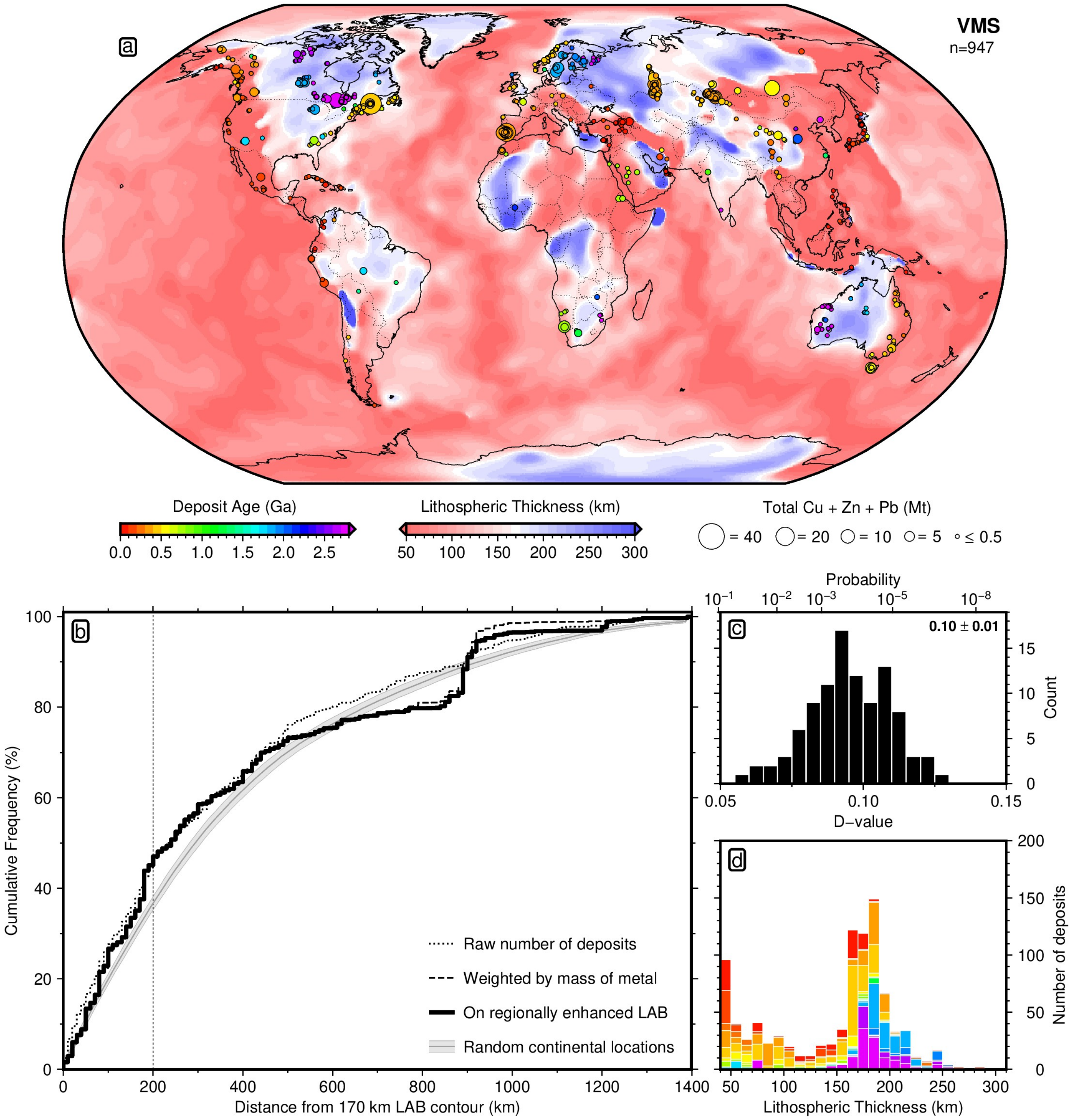

Figure S20: **947 volcanogenic massive sulphide deposits.** (a) LAB derived from SL2013sv tomography model using a calibrated anelasticity parameterisation.[17,15] Circles = deposit locations; area proportional to estimate of total contained mass of metal (MT = megatonnes); unknown deposit size given 0.5 Mt symbol; colour = ore body formation age (billion years); unknown age plotted in grey. (b) Different approaches for generating cumulative distribution functions. Dotted line = simple count of number of deposits with increasing distance from the 170 km contour in global LAB map; dashed line = weighting by contained mass of copper, lead and zinc; solid black line = mass of metal-weighted deposits where Australian LAB has been replaced with regionally enhanced map (Figure S8a); grey line/bounds = mean and standard deviation of 100 sets of equivalent number of randomly drawn continental locations, with respect to regionally enhanced LAB. (c) Histogram of 100 D-values calculated for each random test set and a non-mass-weighted, locally enhanced CDF; inset lists mean and standard deviation of D-values; associated probabilities shown across top. (d) Histogram of deposit occurrence as a function of lithospheric thickness, coloured by deposit age.